Schweizerische Eidgenossenschaft
Confédération suisse
Confederazione Svizzera
Confederaziun svizra

Department of the Environment,
Transport, Energy and Communication DETEC

Swiss Federal Office of Energy SFOE
Energy Research

Final report (public)

ConPEC

Concentrated photoelectrochemical fuel generation: scale-up, on-sun testing, and flexibilization

Date: 19 March 2021

Place: Lausanne

Publisher:
Swiss Federal Office of Energy SFOE
Research Programme Energieforschung
CH-3003 Bern
www.bfe.admin.ch
energieforschung@bfe.admin.ch

Agent:
Laboratory of Renewable Energy Science and Engineering (LRESE)
EPFL
Station 9
CH-1015 Lausanne
www.epfl.ch

Author:
Saurabh Tembhurne, EPFL, saurabh.tembhurne@epfl.ch
Isaac Holmes-Gentle, EPFL, isaac.holmes-gentle@epfl.ch
Clemens Suter, EPFL, clemens.suter@epfl.ch
Sophia Haussener, EPFL, sophia.haussener@epfl.ch

SFOE programme manager: Stefan Oberholzer, stefan.oberholzer@bfe.admin.ch
SFOE contract number: SI/501596-01

Summary

ConPEC was a 3-year research project that targeted the analysis, development and design of a scaled and scalable solar fuel reactor design and solar fuel processing system based on a thermally integrated photoelectrochemical approach operating with concentrated solar irradiation, an approach that was previously demonstrated at the laboratory scale and under laboratory conditions. The project included the integration of this scaled solar reactor into a full solar plant system with all functionally required auxiliary components (such as concentrator, pump, separator) and the assessment of the impact of these auxiliary components on the reactor and system performance. The implemented system was required to reach a kW power scale and was expected to stably operate over multiple days exposed to changing solar irradiation conditions. Furthermore, we aimed at exploring the possibility of the flexible operation of the system (on-sun only, sun-grid hybrid, etc.) and the tunability of the product portfolio (not only including fuel, but also heat and electricity), in order to propose pathways for larger capacity factors and economically competitive operation. Finally, the transferability of the design approach to alternative electrochemical reactions (such as CO_2 reduction) was investigated.

In the framework of the project, we installed a commercial 7m-diameter solar parabolic concentrator on EPFL campus with the potential for 38 kW_{th} input power to the system. We developed a solar reactor with an aperture and photoactive area of 12x12 cm^2, operating at an input power range of ~15 kW. The reactor was designed and manufactured to be able to sustain operation in the focal spot of the solar concentrator, being exposed to solar irradiation fluxes up to 1600 kW/m^2. The reactor was integrated into a complete system that was designed for automated and continuous operation, requiring auxiliary components such as a pump, hydrogen-water and oxygen-water separators (both designed in-house), de-ionizers, and an oxygen compressor. The system was connected to the compressed hydrogen and oxygen storage (20-30 bar) of the micro-grid of the Distributed Electrical Systems Laboratory at EPFL.

The system was exposed to multiple days of operation under variable solar conditions and demonstrated the production of up to 0.46 kg (or 5680 NL) of compressed hydrogen in one day (of 7.77 hours of on-sun operation). The typical operational potential was in the range of 55-60 V and the typical operational current was in the range of 55-62A. For this longest-day scenario, the measured solar-to-hydrogen system efficiency was 6.0%, the solar-to-hydrogen diagnostic device efficiency was 21.2%, and the co-generation solar-to-hydrogen&heat efficiency was 45.1%. These performance characteristics are extremely promising and a startup company was established in early 2020 (https://www.sohhytec.com/), aiming at further scaling and commercializing the system. A public browser-based online interface (https://solardish.epfl.ch/) was developed that allows to follow past and future campaigns of our solar fuel plant online, and is meant as a broad outreach tool to interested parties in academia, industry, government, and the broad public.

The experimental activities were accompanied by the development of a transient and coupled multi-physics solar plant model which allowed for the investigation and quantification of the dynamics of the system. The model results provide detailed insights in the coupled nature of the system, highlight the importance and uniqueness of the thermal integration and how it affects the system dynamics, and quantified the hysteresis in operation when exposed to sudden changes in operating conditions (e.g. changing DNI or flow rates). The model was then used to provide controlling strategies for the operation of the solar plant as well as to propose operational strategies for operation leading to better capacity factors. These studies show that when – for example – hybrid sun-grid operation is considered, the capacity factor can be considerably increased, especially during days with bad weather conditions (i.e. large transients, many clouds). Additionally, the model provided guidelines for the operation for the co-generation of fuel and heat. We were able to show experimentally that the temperature level of the rejected heat was at least in the range of 55°C (with potential for increased temperatures by increasing the insulation of the piping of the system), providing daily ~110 kWh_{th} of renewable heat usable in residential and industrial applications.

Finally, we have shown in the laboratory photoelectrochemical device that CO_2 reduction to CO was possible with the same concentrated integrated photoelectrochemical device design and thermal integration idea, highlighting that potentially the same or similar scaling approaches can be followed.

This project provides one of the first and largest power demonstrations of an integrated photoelectrochemical device operating under concentrated irradiation and utilizing intricate thermal integration. The quantified performance of the overall system gives first evidence on the magnitude of performance reduction associated with all auxiliary but necessary components in a complete solar fuel processing plant system. The experimental data shows that dynamic and robust operation is possible, with the potential to implement advanced controlling and/or operational flexibilization schemes. The 4-days experimental campaign hints at the feasibility of stable longer term operation.

The research contributes to the basic understanding of operating concentrated integrated photoelectrochemical devices, provide a unique platform for the investigation of the long-term performance of concentrated integrated photoelectrochemical devices exposed to realistic operating conditions, and will support the development of a marketable device and complete system. The project provides demonstration of the feasibility of concentrated integrated photoelectrochemical approaches on large scales and at reasonable expenses, and therefore makes a case for the continuation and intensification of photoelectrochemistry research.

Zusammenfassung

ConPEC war ein dreijähriges Forschungsprojekt, das auf die Analyse, Entwicklung und Konstruktion eines skalierten und skalierbaren solaren Brennstoffreaktor-Designs und eines solaren Brennstoffverarbeitungssystems abzielte, das auf einem thermisch integrierten photoelektrochemischen Ansatz basiert, der mit konzentrierter Sonneneinstrahlung arbeitet. Ein Ansatz, der zuvor im Labormaßstab und unter Laborbedingungen demonstriert wurde. Das Projekt umfasste die Integration dieses skalierten Solarreaktors in ein vollständiges Solaranlagensystem mit allen funktionell erforderlichen Hilfskomponenten (wie Konzentrator, Pumpe, Separator) und die Bewertung der Auswirkungen dieser Hilfskomponenten auf die Reaktor- und Systemleistung. Das implementierte System musste eine kW-Leistung erreichen und sollte über mehrere Tage unter wechselnden Sonneneinstrahlungsbedingungen stabil arbeiten. Darüber hinaus zielten wir darauf ab, die Möglichkeit des flexiblen Betriebs des Systems (nur bei Sonneneinstrahlung, Sonnen-Netz-Hybrid usw.) und die Abstimmbarkeit des Produktportfolios (nicht nur einschließlich Brennstoff, sondern auch Wärme und Elektrizität) zu untersuchen, um Wege für größere Kapazitätsfaktoren und einen wirtschaftlich wettbewerbsfähigen Betrieb vorzuschlagen. Schließlich wurde die Übertragbarkeit des Design-Ansatzes auf alternative elektrochemische Reaktionen (wie z.B. CO_2-Reduktion) untersucht.

Im Rahmen des Projekts installierten wir auf dem Campus der EPFL einen kommerziellen Solar-Parabolkonzentrator mit einem Durchmesser von 7 m, der das Potenzial für eine Eingangsleistung von 38 kW_{th} in das System hat. Wir entwickelten einen Solarreaktor mit einer Apertur und photoaktiven Fläche von 12x12 cm^2, der in einem Eingangsleistungsbereich von ~15 kW arbeitet. Der Reaktor wurde so konstruiert und hergestellt, dass er im Brennpunkt des Sonnenkonzentrators betrieben werden kann, wo er solaren Einstrahlungsflüssen von bis zu 1600 kW/m^2 ausgesetzt ist. Der Reaktor wurde in ein Komplettsystem integriert, das für einen automatisierten und kontinuierlichen Betrieb ausgelegt ist und Hilfskomponenten wie eine Pumpe, Wasserstoff-Wasser- und Sauerstoff-Wasser-Separatoren (beide eigens am Labor entwickelt), Deionisatoren und einen Sauerstoffkompressor erfordert. Das System wurde an den Druckwasserstoff- und Drucksauerstoffspeicher (20-30 bar) des Mikronetzes des Labors für verteilte elektrische Systeme (DESL) der EPFL angeschlossen.

Das System wurde mehreren Betriebstagen unter variablen Sonnenbedingungen ausgesetzt und demonstrierte die Produktion von bis zu 0.46 kg (oder 5680 NL) komprimiertem Wasserstoff an einem Tag (von 7.77 Stunden Sonnenbetrieb). Das typische Betriebspotential lag im Bereich von 55-60 V und der typische Betriebsstrom im Bereich von 55-62 A. Bei diesem Szenario mit dem längsten Tag lag der gemessene Solar-Wasserstoff-Systemwirkungsgrad bei 6.0%, der diagnostische Solar-Wasserstoff-Reaktorwirkungsgrad bei 21.2% und der Wirkungsgrad der Solar-Wasserstoff-Wärme-Kopplung bei 45.1%. Diese Leistungsmerkmale sind äußerst vielversprechend, und Anfang 2020 wurde ein Startup-Unternehmen gegründet (https://www.sohhytec.com/), das eine weitere Skalierung und Kommerzialisierung des Systems anstrebt. Es wurde eine öffentliche browserbasierte Online-Schnittstelle (https://solardish.epfl.ch/) entwickelt, die es ermöglicht, vergangene und zukünftige Kampagnen unserer Solarbrennstoffanlage online zu verfolgen, und die als Instrument für eine breite Öffentlichkeitsarbeit für interessierte Parteien in Wissenschaft, Industrie, Regierung und die breite Öffentlichkeit gedacht ist.

Die experimentellen Aktivitäten wurden von der Entwicklung eines transienten und gekoppelten multiphysikalischen Solaranlagenmodells begleitet, das die Untersuchung und Quantifizierung der Dynamik des Systems ermöglichte. Die Modellergebnisse liefern detaillierte Einblicke in die gekoppelte Natur des Systems, heben die Bedeutung und Einzigartigkeit der thermischen Integration und deren Einfluss auf die Systemdynamik hervor und quantifizierten die Hysterese im Betrieb, wenn das System plötzlichen Änderungen der Betriebsbedingungen (z.B. wechselnde DNI oder Durchflussraten) ausgesetzt ist. Das Modell wurde dann verwendet, um Regelungsstrategien für den Betrieb der

Solaranlage bereitzustellen und um Betriebsstrategien für den Betrieb vorzuschlagen, die zu besseren Kapazitätsfaktoren führen. Diese Studien zeigen, dass - wenn z.B. ein hybrider Sonnen-Netz-Betrieb in Betracht gezogen wird - der Kapazitätsfaktor erheblich erhöht werden kann, insbesondere an Tagen mit schlechten Wetterbedingungen (d.h. große Transienten, starke Bewölkung). Darüber hinaus lieferte das Modell Richtlinien für den Betrieb bei der Kraft-Wärme-Kopplung von Brennstoff und Wärme. Wir konnten in der Tat experimentell zeigen, dass das Temperaturniveau der abgeleiteten Wärme mindestens im Bereich von 55°C lag (mit Potenzial für erhöhte Temperaturen durch eine verstärkte Isolierung der Rohrleitungen des Systems), wodurch täglich ~110 kWh_{th} erneuerbarer Wärme zur Verfügung stehen, die in Wohn- und Industrieanwendungen genutzt werden kann.

Schließlich haben wir im photoelektrochemischen Laboratorium gezeigt, dass eine CO_2-Reduzierung zu CO mit dem gleichen konzentrierten integrierten photoelektrochemischen Gerätedesign und der gleichen Idee der thermischen Integration möglich ist, wobei hervorgehoben wurde, dass potenziell die gleichen oder ähnliche Skalierungsansätze verfolgt werden können.

Dieses Projekt bietet eine der ersten und größten Leistungsdemonstrationen einer integrierten photoelektrochemischen Vorrichtung, die unter konzentrierter Bestrahlung arbeitet und eine komplizierte thermische Integration nutzt. Die quantifizierte Leistung des Gesamtsystems gibt einen ersten Hinweis auf das Ausmaß der Leistungsreduzierung, die mit allen Hilfs-, aber notwendigen Komponenten in einem kompletten System einer Solarbrennstoff-Verarbeitungsanlage verbunden ist. Die experimentellen Daten zeigen, dass ein dynamischer und robuster Betrieb möglich ist, mit dem Potential, fortschrittliche Steuerungs- und/oder Betriebsflexibilisierungsansätze zu implementieren. Die 4-tägige experimentelle Kampagne deutet auf die Machbarkeit eines stabilen längerfristigen Betriebs hin.

Die Forschung trägt zum grundlegenden Verständnis des Betriebs von konzentrierten integrierten photoelektrochemischen Vorrichtungen bei, bietet eine einzigartige Plattform für die Untersuchung der Langzeitleistung von konzentrierten integrierten photoelektrochemischen Vorrichtungen unter realistischen Betriebsbedingungen und wird die Entwicklung einer marktfähigen Vorrichtung und eines kompletten Systems unterstützen. Das Projekt bietet eine Demonstration der Machbarkeit konzentrierter integrierter photoelektrochemischer Ansätze in großem Maßstab und zu vertretbaren Kosten und spricht sich daher für die Fortsetzung und Intensivierung der photoelektrochemischen Forschung aus.

Résumée

ConPEC était un projet de recherche de 3 ans qui visait l'analyse, le développement et la conception d'une conception de réacteur à combustible solaire à l'échelle et modulable et d'un système de traitement du combustible solaire basé sur une approche photoélectrochimique intégrée thermiquement fonctionnant avec une irradiation solaire concentrée, une approche qui a été démontrée précédemment à l'échelle du laboratoire et dans des conditions de laboratoire. Le projet comprenait l'intégration de ce réacteur solaire à échelle réduite dans un système de centrale solaire complet avec tous les composants auxiliaires nécessaires au fonctionnement (tels que concentrateur, pompe, séparateur) et l'évaluation de l'impact de ces composants auxiliaires sur le rendement du réacteur et du système. Le système mis en œuvre devait atteindre une puissance de l'ordre du kW et devait fonctionner de manière stable pendant plusieurs jours exposés à des conditions d'irradiation solaire changeantes. En outre, nous avons cherché à explorer la possibilité d'un fonctionnement flexible du système (sur le soleil uniquement, hybride soleil-réseau, etc.) et la possibilité d'adapter le portefeuille de produits (comprenant non seulement le combustible, mais aussi la chaleur et l'électricité), afin de proposer des voies pour des facteurs de capacité plus importants et un fonctionnement économiquement compétitif. Enfin, la transférabilité de l'approche de conception à des réactions électrochimiques alternatives (telles que la réduction du CO_2) a été étudiée.

Dans le cadre de ce projet, nous avons installé un concentrateur solaire parabolique commercial de 7 m de diamètre sur le campus de l'EPFL, avec un potentiel de 38 kW_{th} de puissance d'entrée dans le système. Nous avons développé un réacteur solaire avec une ouverture et une surface photoactive de 12x12 cm^2, fonctionnant à une puissance d'entrée de ~15 kW. Le réacteur a été conçu et fabriqué pour pouvoir fonctionner dans le point focal du concentrateur solaire, étant exposé à des flux d'irradiation solaire allant jusqu'à 1600 kW/m^2. Le réacteur a été intégré dans un système complet conçu pour un fonctionnement automatisé et continu, nécessitant des composants auxiliaires tels qu'une pompe, des séparateurs hydrogène-eau et oxygène-eau (tous deux conçus en interne), des dé-ioniseurs et un compresseur d'oxygène. Le système a été connecté au stockage d'hydrogène et d'oxygène comprimé (20-30 bar) du micro-réseau du Laboratoire des systèmes électriques distribués de l'EPFL.

Le système a été exposé à plusieurs jours de fonctionnement dans des conditions solaires variables et a démontré la production de jusqu'à 0.46 kg (ou 5680 NL) d'hydrogène comprimé en un jour (sur 7.77 heures de fonctionnement au soleil). Le potentiel opérationnel typique se situait dans la plage de 55-60 V et le courant opérationnel typique dans la plage de 55-62A. Pour ce scénario de journée la plus longue, l'efficacité mesurée du système solaire-hydrogène était de 6.0%, l'efficacité diagnostic du réacteur solaire-hydrogène était de 21.2%, et l'efficacité de la cogénération solaire-hydrogène-chaleur était de 45.1%. Ces caractéristiques de performance sont extrêmement prometteuses et une start-up a été créée au début de 2020 (https://www.sohhytec.com/), dans le but de poursuivre la mise à l'échelle et la commercialisation du système. Une interface en ligne basée sur un navigateur public (https://solardish.epfl.ch/) a été développée pour permettre de suivre en ligne les campagnes passées et futures de notre centrale à combustible solaire, et est conçue comme un outil de sensibilisation à grande échelle pour les parties intéressées dans les universités, l'industrie, le gouvernement et le grand public.

Les activités expérimentales ont été accompagnées par le développement d'un modèle de centrale solaire multi-physique transitoire et couplé qui a permis d'étudier et de quantifier la dynamique du système. Les résultats du modèle fournissent des informations détaillées sur la nature couplée du système, soulignent l'importance et le caractère unique de l'intégration thermique et la manière dont elle affecte la dynamique du système, et quantifient l'hystérésis en fonctionnement lorsqu'elle est exposée à des changements soudains des conditions de fonctionnement (par exemple, changement de DNI ou de débit). Le modèle a ensuite été utilisé pour fournir des stratégies de contrôle pour l'exploitation de la

centrale solaire ainsi que pour proposer des stratégies opérationnelles d'exploitation conduisant à de meilleurs facteurs de capacité. Ces études montrent que lorsque - par exemple - le fonctionnement hybride du réseau solaire est envisagé, le facteur de capacité peut être considérablement augmenté, en particulier pendant les jours où les conditions météorologiques sont mauvaises (c'est-à-dire les grands transitoires, les nuages d'origine humaine). En outre, le modèle a fourni des lignes directrices pour l'exploitation de la cogénération de carburant et de chaleur. Nous avons en effet pu montrer expérimentalement que le niveau de température de la chaleur rejetée était au moins de l'ordre de 55°C (avec un potentiel d'augmentation des températures en augmentant l'isolation de la tuyauterie du système), fournissant par jour ~110 kWh_{th} de chaleur renouvelable utilisable dans des applications résidentielles et industrielles.

Enfin, nous avons montré en laboratoire que la réduction du CO_2 en CO était possible avec la même conception de dispositif photoélectrochimique intégré concentré et la même idée d'intégration thermique, ce qui souligne que des approches d'échelle potentiellement identiques ou similaires peuvent être suivies.

Ce projet constitue l'une des premières et des plus grandes démonstrations de puissance d'un dispositif photoélectrochimique intégré fonctionnant sous irradiation concentrée et utilisant une intégration thermique complexe. La performance quantifiée du système global donne une première preuve de l'ampleur de la réduction de performance associée à tous les composants auxiliaires mais nécessaires dans un système complet d'usine de traitement de combustible solaire. Les données expérimentales montrent qu'un fonctionnement dynamique et robuste est possible, avec la possibilité de mettre en œuvre des schémas avancés de contrôle et/ou de flexibilité opérationnelle. La campagne expérimentale de 4 jours laisse entrevoir la faisabilité d'un fonctionnement stable à plus long terme.

La recherche contribue à la compréhension fondamentale du fonctionnement des dispositifs photoélectrochimiques intégrés concentrés, fournit une plateforme unique pour l'étude des performances à long terme des dispositifs photoélectrochimiques intégrés concentrés exposés à des conditions de fonctionnement réalistes, et soutiendra le développement d'un dispositif commercialisable et d'un système complet. Le projet démontre la faisabilité des approches photoélectrochimiques intégrées concentrées à grande échelle et à des coûts raisonnables, et plaide donc en faveur de la poursuite et de l'intensification de la recherche en photoélectrochimie.

Contents

List of abbreviations

ALD	Atomic Layer Deposition
CIPEC	Concentrated Integrated Photoelectrochemical
CSP	Concentrated Solar Power
DESL	Distributed Electrical Systems Laboratory
DHI	Diffuse Horizontal Irradiance
DNI	Direct Normal Irradiance
EC	Electrochemical
EPFL	Ecole Polytechnique Fédérale de Lausanne
GHI	Global Horizontal Irradiance
HAZOP	Hazard and Operability
HX	Heat Exchanger
IPEC	Integrated Photoelectrochemical
LPM	Liters Per Minute
LRESE	Laboratory of Renewable Energy Science and Engineering
MPP	Maximum Power Point
NL	Normal Liter
PEC	Photoelectrochemical
PEM	Proton Exchange Membrane
PID	Process Implementation Diagram
PV	Photovoltaics
SFOE	Swiss Federal Office of Energy
TSP	Temperature Stationary Point

1 Introduction

The energy economy is facing a significant challenge to transition towards sustainable and renewable energy resources and away from its fossil fuel dominated characteristics (currently ~82% non-renewable resources[†]). The scale of the energy sector is significant, final consumption is in the range of ~13 TW, with an anticipated growth of up to ~25% for the 2040-time horizon. The final consumption currently consists in ~20% electricity and the remainder in combustible fuels (coal, oil products, gas, biofuels) for transportation and heat. While the electrification fraction is expected to increase, heat and fuel will remain dominant and sustainable and renewable approaches for their production and conversion have to be found, demonstrated, scaled and implemented.

The potential of renewable energy resources has been assessed in detail and solar energy has emerged as one of the resources with the largest and most significant potential [1]. Solar energy for electricity production via photovoltaics (PV) or concentrated solar power (CSP) is already commercial, installed on significant scale (505 GW PV capacity installed, 5.5 GW CSP capacity installed[‡]), and economically competitive. Similarly, solar energy for low-temperature heat via solar collectors is already commercial and installed on a large scale (480 GW_{th} solar collector capacity installed[‡]). On the other hand, solar fuel processing (not considering biomass) are not yet well established. There are effectively two major approaches for solar fuels: solar thermochemical and photoelectrochemical (PEC) approaches. The former makes use of concentrated radiation to provide high-temperature heat for a thermochemical reaction (for example the reduction and oxidation of metal-oxides for – in net – the splitting of water) while the latter makes use of the photon energy to generate charge carriers to drive electrochemical reactions (for example the electrolysis of water). Both approaches have shown interesting efficiencies, at reasonable scales, with challenges in the stability [2], and can be considered complementing approaches to large-scale production of solar fuels. Here, we will focus on the scaling, design, and demonstration of a thermally integrated photo-electrochemical approach.

Photoelectrochemistry requires a semiconducting material that absorbs the solar radiation to generate electron-hole pairs that are transported to and separated at the semiconductor-electrolyte interface and subsequently used in an anodic oxidation reaction of water for oxygen evolution and a cathodic reduction of protons for hydrogen evolution. The electrolyte provides also the ionic path between the anode and cathode for the transport of protons (in the acidic case) or hydroxyl ions (for the alkaline case). This simplest configuration of a PEC approach has been demonstrated 50 years ago [3]. In order to increase efficiency, reduce degradation, and reduce the reliance on rare and expensive materials, current designs of PEC cells incorporate multiple photoabsorber materials, multiple co-catalysts, or protective layers. The design and optimization of such a device has become more complex but has enabled laboratory-scale device demonstrations with efficiencies above 15% [4], [5] (see also: http://specdc.epfl.ch/). Different levels of integration of the photoabsorber, co-catalysts and electrolyte are possible and have been demonstrated [5], [6]. Stability and robustness of the designs have more recently been identified as the most severe challenges, limiting the commercial implementation of such devices [4]. One way to partially overcome the stability challenge is the introduction of protective layers, effectively burying the photoabsorber and moving it away from the electrolyte interface [7]. Designs that are burying the photoabsorber away from the electrolyte are integrated photovoltaics plus electrolyzer devices [6]. The integration of the two components, however, has shown to be advantageous from a device efficiency point of view, given that thermal synergies can be exploited [5]. However, thermal management has to be carefully developed and controlled to ensure an operational device.

[†] Statistics in this paragraph from IEA's Key World Energy Statistics 2018

[‡] Statistics from REN21 Renewable 2019 Global Status Report

Techno-economic [8], [9] and environmental [10]–[12] studies of PEC approaches have predicted that such devices and systems can indeed be designed, implemented and scaled in a sustainable and cost-competitive manner. Specifically, the utilization of concentrated radiation might provide a crucial economic advantage while also allowing for the utilization of rarer (but high performing) materials [8]. Ultimately, concentrated irradiation enables this economically important high current and power densities. However, large current density operation requires the management of disproportionately higher losses in a PEC device, a challenge that needs to be carefully addressed through dedicated PEC device modeling and subsequent design [5], [13].

The largest scale demonstration of a solar fuel processing device is in the range of 30 W (output power) [5]. No scalable demonstration has been implemented up to now. However, scalability is essential if an energy transition in the TW-scale is targeted. Scaling of PEC devices is also challenging, given that the typical scaling approaches of the PV or the electrolyzer communities cannot simply be translated and applied. Instead, new scaling guidelines have to be developed that consider the combined multi-physical nature of the photo-driven electrochemical process. Additionally, the step from a laboratory-scale demonstration to a solar fuel processing system requires the consideration, design and incorporation of system-relevant peripherals (concentrator, pumps, compressors, separators, etc.) in addition to carefully placed diagnostics tools (temperature and pressure sensors, etc.) while also developing accurate measurement tools and procedures (for example flux measurements). Finally, performance analysis and optimization on the system level open new pathways for co-generation ideas that have not yet been investigated.

In this project, we have designed, implemented, characterized and operated a scalable thermally integrated PEC system that is able to produce up to 0.5 kg of hydrogen during a nice, sunny day. The scaled design has been based on our laboratory scale demonstration [5] with the corresponding extension to system level. Characterization methods and in-situ performance characteristics have been developed and recorded to provide access to system performance and to identify the most critical components. The recorded data is available to the public via a dedicated, developed public interface (https://solardish.epfl.ch/). The design and operation of the system has been supported by a transient multi-physical system model. The solar plant and the model have then been used to explore operational and product flexibilization approaches, considering possible controlling approaches and co-generation schemes (simultaneous production of fuel plus heat and electricity production). Finally, the chemistry flexibilization has been assessed at the laboratory scale for CO_2 reduction to CO, showing the possibility to translate this chemistry into the solar plant.

2 Context

2.1 Background / State of the art

Direct conversion of solar energy and water (or other reactants such as CO_2 or N_2) into chemical energy in the form of hydrogen via PEC processes is one viable route for renewable fuel processing, for chemical commodities processing, and for energy storage. Complicated and coupled multi-physics processes, which happen on multiple time and spatial scales, govern the functionality of PEC devices. In order for such a device to have a significant effect on our energy economy, it has to simultaneously fulfill four requirements: it has to be efficient, robust, economically competitive, and sustainable.

Macroscopic system modeling suggested that PEC devices operating with concentrated irradiation and current concentration can provide a competitive and sustainable approach to PEC fuel generation [8]. However, the implementation of a functional PEC device operating at concentrated irradiation was a challenge given the high fluxes, large thermal energy density, and the elevated currents with the corresponding losses. Advanced, coupled multi-physics modelling allowed for the feasibility assessment of such an approach [14] and the subsequent design of a laboratory-scale demonstrator proved that the concept can be implemented and the operational condition and performance are competitive (Figure 2.1) [5]. The concept ultimately utilized a buried junction approach [7] to ensure sufficient operational stability. Interestingly, the buried junction design allowed for an intricate thermal design, providing a synergy that enabled larger efficiencies while enabling high current density operation in the first place [5]. Effectively, the water flow acted not only as reactant but also as a heat transfer medium, enabling the cooling of the photoabsorber while pre-heating the reactant that is then used in the electrochemical reaction, overall increasing the efficiency (Figure 2.2a). The efficiency benefit is owed to the use of thermal input energy from the long-wavelength photons (that are directly absorbed in the reactant) and thermalization losses in the photoabsorber (that are removed by forced convection). The resulting elevated temperature operation in the electrochemically active part allows for the reduction in the overpotentials, effectively accepting operation at larger current densities while maintaining high efficiencies (Figure 2.2b).

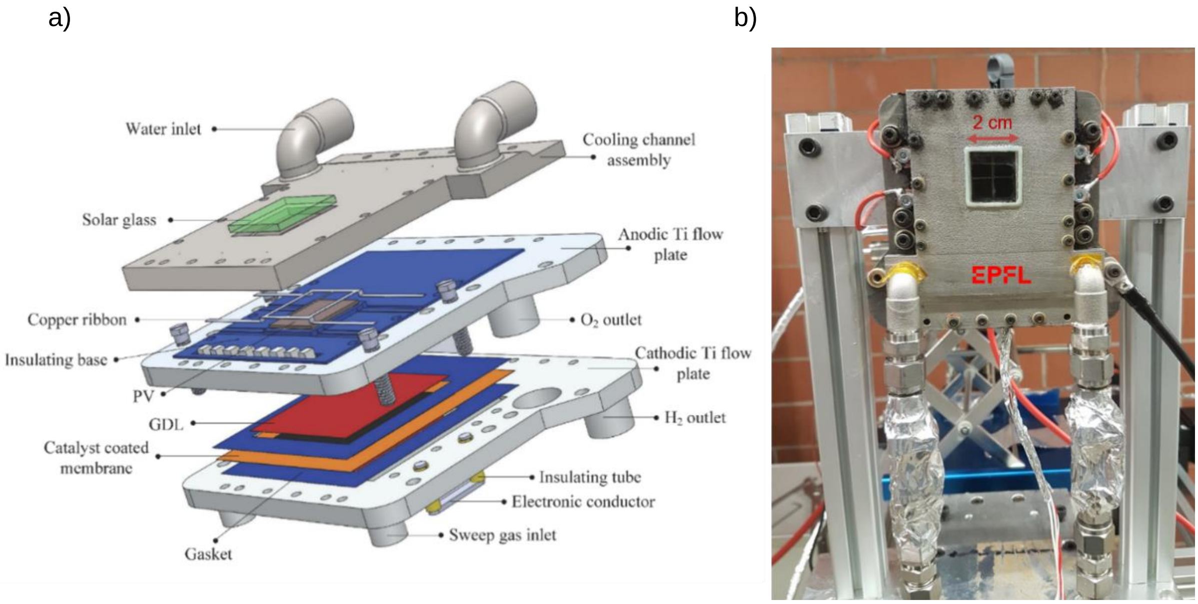

Figure 2.1. a) CAD drawing of the integrated PEC device that utilizes concentrated solar radiation (entering through the top window). b) Photo of the Theoretical efficiency limit as a function of operational current density (or irradiation concentration) for various bandgaps (color of line). Adapted from [5].

Testing in our high-flux solar simulator (characteristics of our high-flux solar simulator can be found elsewhere [15]) demonstrated a solar-to-hydrogen device efficiency of 17% at a record large power (27 W output power) and large current densities (~1A/cm^2) [5]. This proof of concept is a first step towards a more practical device which can be economically competitive. In order to get there, such a device needs to be scaled, tested under realistic on-sun conditions, characterized in detail, and the economic competitiveness and capacity factor need to be increased (for example by targeting other chemical reactions and products, i.e. chemical flexibilization, and by additionally utilizing the heat and electricity, and by running dark electrolysis during the night, i.e. operational and product flexibilization).

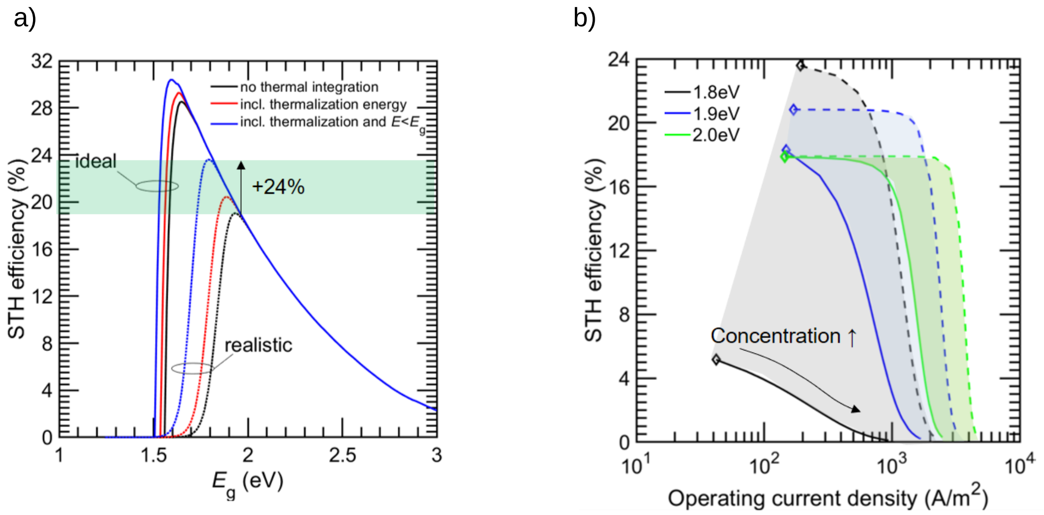

Figure 2.2. a) Theoretical solar-to-hydrogen efficiency as a function of single absorber bandgap in an ideal (solid) and real (dotted) configuration in a thermally non-integrated (black), intermediately integrated (red) and ultimately integrated (blue) configuration. b) Theoretical efficiency limit as a function of operational current density (or irradiation concentration) for various bandgaps (color of line). Adapted from [5].

2.2 Motivation of the project

The motivation of the project is the desire to develop and demonstrate a scalable and scaled solar fuel processing system. This includes a power-scale that clearly goes beyond the laboratory scale demonstration of ~100 W, that is stable enough to survive multiple months of operation, and the design of a complete system that considers not only the device but also the operationally necessary auxiliary components (such as concentrator, pump, separator etc.) and how they might affect the dynamics and operation. This demonstration requires a full understanding of the dynamic multi-physical nature of the device and system processes that is coupled through the thermal integration, a novelty of this device and system. Additionally, the understanding of how the system can be operated in a more flexible way to improve performance and capacity factor, to co-generate multiple product, and to explore the translatability of the device and system design approach towards other electrochemical reactions (such as CO_2 reduction). Finally, the collection of performance and operational data of the system over multiple days, exposed to a large variety of operational conditions, is targeted in order to show the robustness of the system operation as well as to develop benchmarks for performance comparison. Ultimately the technology readiness level of the system should be increased to provide a more practical and scalable system design that can eventually – with the aid of partners from the private sector (for example a startup) – be brought to the energy market, which is read for sustainable, renewable and scalable solutions addressing the need for non-electricity energy services.

2.3 Goals

The project aims at designing, developing, and implementing of a concentrated integrated PEC device in the kW power scale and testing it under realistic on-sun conditions. This will require the design and implementation of a scaled device prototype, its mounting into the focal spot of a commercial parabolic solar concentrator, and its integration into a complete system with various auxiliary system components (concentrator, pump, separators, compressor, etc.). Furthermore, once successfully implemented, methods for the accurate characterization of the system need to be developed (flux measurements, production rate measurements, efficiency predictions, etc.) and the required diagnostic tools calibrated and installed. Safety and testing protocols need to be developed so as to ensure automated and safe operation and to provide reproducible long-term testing data, potentially available in real time to the researchers and community. Finally, the device design will be tested for increased flexibility in products, this includes the use of heat and electricity, the use of the device also under strong transients or dark conditions (night, where little to no solar irradiation is available), and potentially the testing for alternative electrochemical reactions (for example CO_2 reduction). The implemented and tested system should provide evidence for an efficient, robust and cost-competitive solar fuel processing plant in the hope that its scaling and commercialization will be continued partially also in collaboration with private partners.

Four significant milestones were defined related to the three work packages (WP1: device scaling, WP2: device characterization, and WP3: device flexibilization) in order to ensure that the project goals can be achieved. Milestone 1 (achieved) marks the successful demonstration of the scaled CPEC device in the dish system, milestone 2 (achieved) marks reaching a scaled device performance close to the performance of the lab-scale prototype (namely in the range of 15% solar-to-fuel device efficiency), milestone 3 (achieved for multiple days) marks the successful characterization of the long-term operation, and milestone 4 (achieved) marks the achievement of a system flexibilization path. Three deliverables are defined, which mark a public summary of the achievements in the three work packages.

3 Design overview

3.1 Integrated Photo-Electrochemical Reactor

The integrated photo-electrochemical (IPEC) reactor comprises of a flux homogenizer, a photovoltaic (PV) component, an electrochemical (EC) component, and an intricate fluidic and electric coupling. This IPEC reactor carries out the multi-physical processes required in a functional PEC device. The homogenizer specifically aims at homogenizing the concentrated sunlight (coming from the parabolic concentrator and typically in Gaussian distribution), the PV component absorbs this homogenized concentrated sunlight, thereby generating electrical charges, which are utilized in the EC component for the electrolysis of water to produce hydrogen and oxygen. Furthermore, a protective shield, reactor enclosing and holding boxes, valves, relays and sensors complete the practical implementation of the reactor.

The main considerations while designing and implementing the IPEC reactor were:

1. The reactor has to be as lightweight and dense as possible
2. The fluidic (particularly water flow related) channels and connections within the reactor have to cause as low as possible pressure drop
3. The reactor enclosing should be able to withstand stray concentrated irradiation coming from the imperfections in the parabolic dish concentrator

CAD modelling was used to pre-verify the layout, volume and weight. The CAD schematic is shown in Figure 3.1.

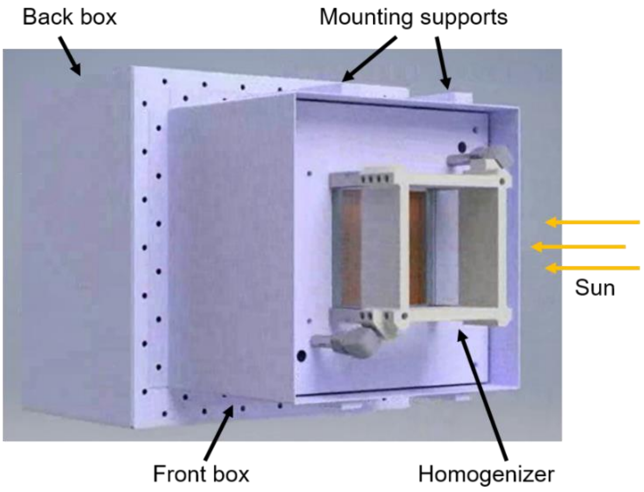

Figure 3.1. 3D rendering of CAD model showing the external view (front side).

The reactor holder has been designed with a “box on box” construction. The enclosure boxes were designed in-house and custom made at EPFL’s mechanical workshop. On the outside (top side) of the front box, the homogenizer is mounted which allows the incoming concentrated sunlight, after getting homogenized, to enter the reactor and fall on the photoactive area of the PV component.

The water acts as reactant as well as coolant, the specialty and novelty in this system design, enabling thermal integration between the various components of the reactor and providing a performance advantage. The oxygen stream has a significant quantity of liquid water (as our input water flow rate is much higher than the stoichiometric requirements). This excess water is evacuated with the oxygen product down to a custom-designed liquid-gas separator while passing through a heat exchanger loop for extracting the heat and recirculation back through the system. This ensure maximum use of the water resource.

The electrical connection layout allows for dynamic change of separated mode operation of the components as well as integrated mode operation. The realization and implementation of the complete reactor is shown in Figure 3.2.

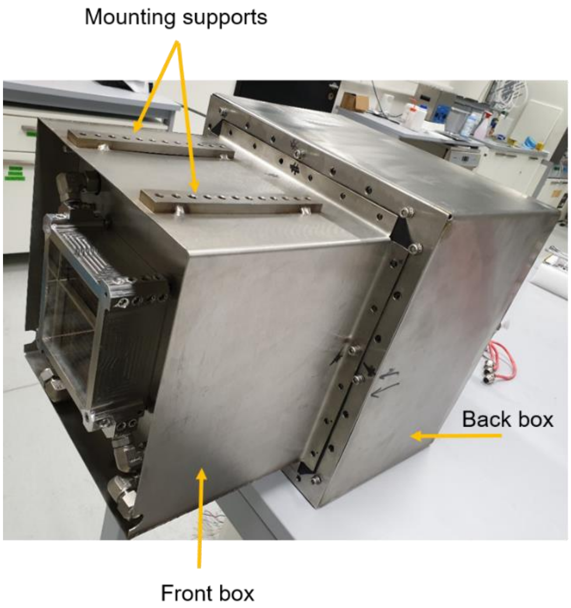

Figure 3.2. Photos showing the isometric view, of the integrated reactor.

The PV component of the integrated-reactor is triple junction III-V material based. The electrochemical component of the reactor is PEM (proton-exchange-membrane) based. The homogenizer is a kaleidoscope-like design. The design was such that the homogenizer can be manufactured conveniently, has enhanced heat removal characteristics, and is lightweight. The measured flux maps of the solar parabolic dish indicated that the concentrated irradiation is not fully focused within the homogenizer area. To protect the key components from stray irradiation, we used an external protective (actively cooled) shield.

The fully assembled reactor mounted at the parabolic concentrators focus (under operation) is shown Figure 3.3.

Figure 3.3. The picture of the integrated photo-electrochemical reactor mounted at the focal spot of the parabolic dish concentrator is shown in operation.

3.2 System design

The Process Flow Diagram shown in Figure 3.5, shows the high-level overview of material flow and energy flow between unit processes. The system comprises an input tap water connection, water tank, water pump, water de-ionizers, integrated photo-electrochemical reactor, liquid-liquid heat exchangers, liquid-gas separators, oxygen compressor, and storage cylinders for oxygen and hydrogen.

The overall operational process of the system is described as follows: The tap water from the water tank is pumped by the water pump via deionizers to the integrated photo-electrochemical reactor at the focal spot of the parabolic dish. The parameters such as temperature, pressure, conductivity and flow rates are measured in real time in this water feeding line. Then the parabolic concentrator starts tracking the sun and hence concentrates the sunlight on the integrated reactor setup. The reactor then generates Oxygen stream (which also has significant liquid water) and Hydrogen stream (which has water vapour) using the sunlight, both of which flow down to their respective liquid-gas separator units. The oxygen stream is passed through a set of liquid-liquid heat exchangers to extract the heat out of this stream. The dry streams following the liquid-gas separators flow through a setup of temperature, pressure and flow rate measurement before finally entering the storage tanks. The oxygen is passed via a compressor (to compress to 30 bars) before storing in the tanks. Hydrogen comes pre-compressed (i.e. compressed at the reactor) from the reactor.

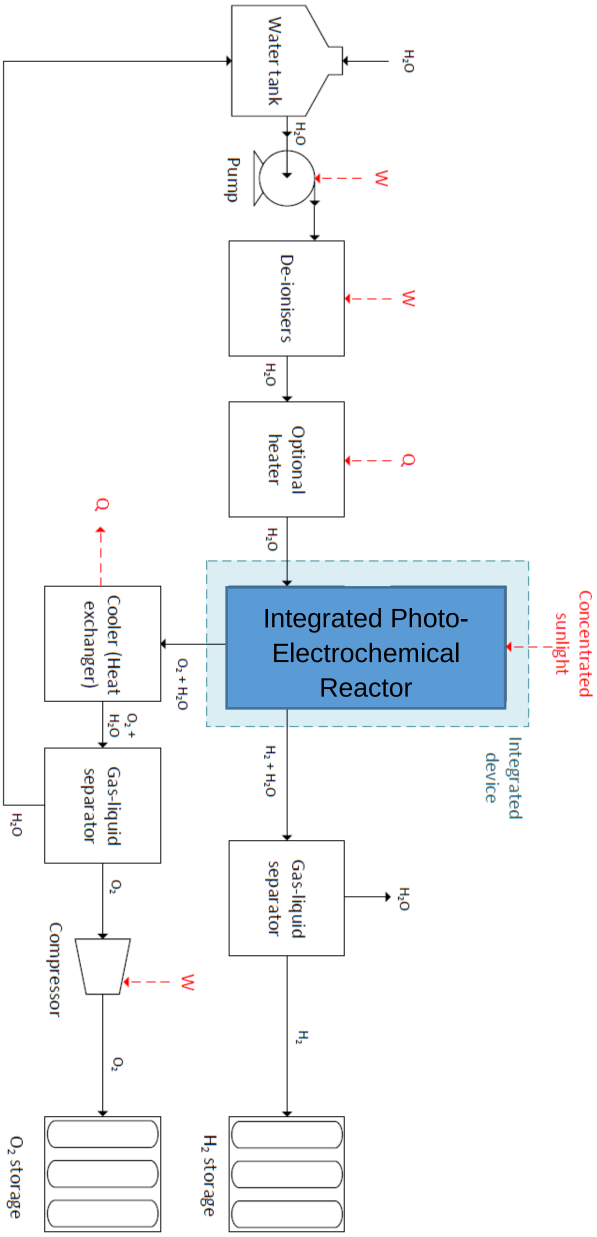

Figure 3.4. Process Flow Diagram (PFD) showing the unit processes of the system and the material and energy flows between them.

3.3 Installation of parabolic dish, system components, piping, and electronics

3.3.1 Solar dish site selection

Site selection was completed during the start of the project (see Figure 3.5) and was chosen for its high availability of solar light not shadowed by adjacent buildings and for the proximity to facilities made available to us. For example, DESL micro-grid facility provides us access to their gas storage tanks which permits integration into their micro-grid network, and the solar pyranometer located on the building of the Solar Energy and Building Physics Laboratory. This pyranometer data is used for real-time DNI measurements.

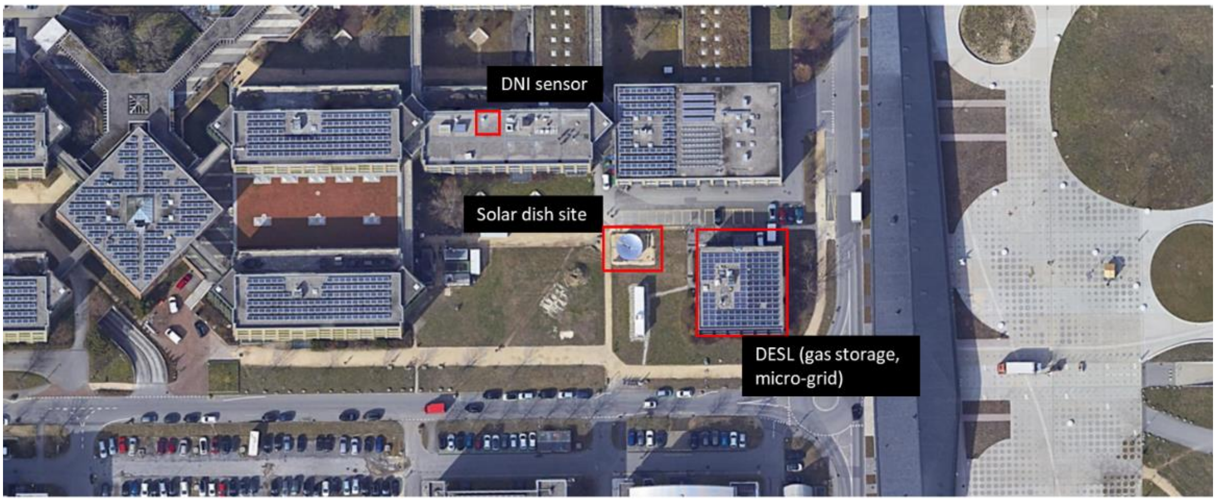

Figure 3.5. Site of solar dish parabola, *Google Earth*, earth.google.com/web/.

3.3.2 System installation

The realization and implementation of the system at the main parabolic concentrator site and at the storage site is shown in Figure 3.6a and 3.6b, respectively.

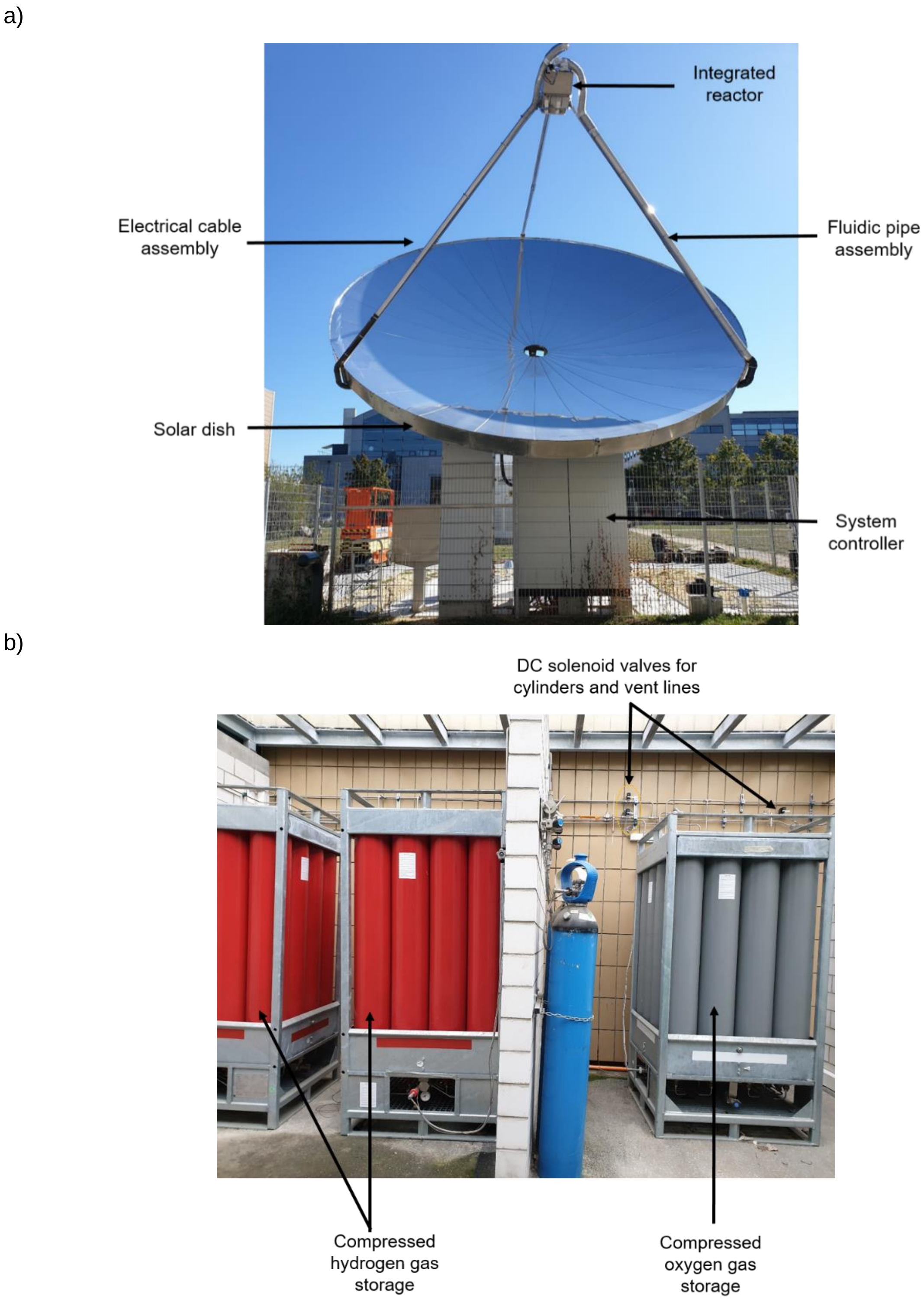

Figure 3.6. a) Photo of the demonstration site (Northside view) showing the parabolic dish, integrated reactor, legs with electrical and fluidic pipe assemblies, system controller, and view of all additional system peripherals. b) Photo of the storage area showing the hydrogen (red) and oxygen (grey) cylinders for storing compressed (20-30 bar) output gases along with piping lines and various sensors.

3.3.3 Weight considerations

Given the novel nature of this project, we had to modify the dish peripherals (e.g. its pipes and receiver area). Our integrated reactor is heavier than the thermal receiver supplied by the dish manufacturer. Additionally, we installed extra pipes and electrical cables on the three supporting legs of the dish. Therefore, a re-evaluation of the permissible weight had to be undertaken. The structural integrity of the dish under the increased reactor weight was successfully verified via two methods (shown in Figure 3.7):

1. Experimental weight testing: measuring of deformation of receiver box under increasing load (Figure 3.7a)
2. Computational analysis of stress in dish legs and mounting brackets under reactor weight load (using Autodesk Inventor stress analysis tool, Figure 3.7b).

The computational analysis showed a maximum stress of 100 MPa. Considering a maximum ultimate tensile strength of 500 MPa for steel, the safety factor is 5. Thus, the mechanical stability is given. A deflection of 1 mm per 5 kg of weight loading has been measured at the receiver area of the solar dish. A longer term (48 hours) test has additionally been conducted at weight loading of 80 kg (which is the total weight of our reactor and other components at the receiver) resulting in a maximum deflection of 16 mm, which confirmed the structural integrity of the supporting legs of the dish.

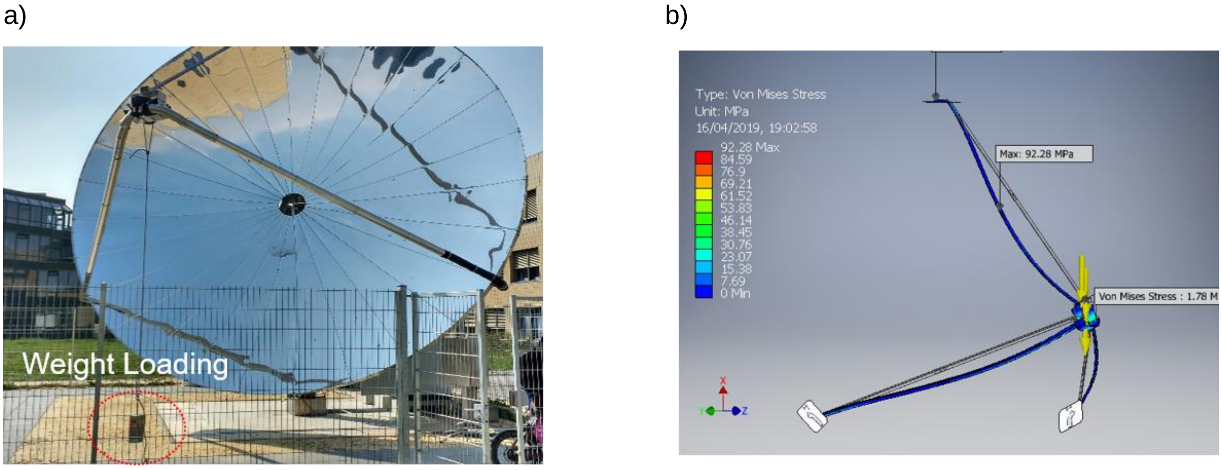

Figure 3.7. a) Photo showing the experimental method for measuring the deflection of the reactor area under weight load. b) Calculated von Mises stress (in MPa) and deflection in the steel legs and mounting brackets under gravity and a load representative of the reactor unit (in Autodesk Inventor). The boundary conditions specified were fixed structural constraints at the bolt holes at the bottom of the legs and 100 N load on each of 4 bolt holes in the reactor mounting bracket.

3.4 Design of auxiliary components

3.4.1 Water-oxygen separator

Due to the pilot scale size of the demonstrator, a custom oxygen-water separator was required as it required a larger capacity than laboratory scale equipment but a smaller capacity than typical industrial scale equipment. Therefore, the separator was designed according to the maximum flowrates of water and oxygen achievable where the separation of the two phases occurs by gravitational separation.

In order to support and validate the design, and to provide estimates for control tuning parameters, a process model of the system was simulated. We built a mixed differential-algebraic model which was numerically solved in gPROMS to study the complex response. The model allowed us to correctly size the control valve parameters as well as provide an initial guess for experimental PID control loop tuning.

3.4.2 Water-hydrogen separator

The hydrogen-water separator is less complex to design than the oxygen-water separator as it deals with lower flowrates of liquid and so can utilize commercial compressed gas filters.

3.5 Process control and monitoring

Process monitoring and control ensures stable automated operation and is an integral part of system design. This was implemented in LabVIEW programming language (from National Instruments).

The structure of the process control and monitoring script is as follows. Each measured process parameter is monitored and saved to a local database. The inbuilt monitoring and alarms system from LabVIEW is used to identify deviations from normal process operation and signal for an intervention to be made (e.g. temporary shutdown). Such control actions are broken down into discrete individual steps such as a valve opened/closed, flowrate set point modified or compressor power relay activated etc. In this way, complex control actions such as the automated start-up and shut down of the system can be achieved. A human-machine interface was developed in order for the process operator to view, request status changes and manually control the system

3.6 Safety analysis

3.6.1 HAZOP study

A hazard and operability study (HAZOP) identifies critical hazards of a chemical process in a systematic and exhaustive manner by investigating a multitude of failure pathways, suggests key risk mitigation strategies and defines which process variables (e.g. temperatures, pressures, concentrations etc.) are essential for safety monitoring. The HAZOP study was completed and multiple safety improvements to the process have since been implemented, with the approval of the EPFL safety department (DSPS).

For every pipe and process equipment (vessel, valve, heat exchanger etc.), a guide word (more, less, as well as etc.) is applied to a certain parameter (e.g. flow, pressure) which gives a specific deviation from normal operation in the component in question (e.g. no flow in heat exchanger). The possible causes for such a deviation are explored and the incident followed to its logical conclusion(s) to elucidate the consequences. Finally, existing safeguards are listed and new safeguards are suggested.

Utilizing the HAZOP study to find the key process parameters that must be monitored, we defined operational states of the system based on logical conditions. For example, if a minor deviation from normal operation is detected, the process operator will get a warning alert, whereas if the deviation is major, the process will automatically shut-down. Low and high alarms are triggered if the process variable is below or above a critical value.

3.6.2 Preventing undesirable solar dish reflections

Due to the location of the solar hydrogen demonstrator and its proximity to workplace buildings, extra care was required to ensure that solar dish reflections do not disturb office workers when the dish in an upright maintenance orientation. A more hazardous situation can occur if the dish is in a vertical maintenance position (e.g. during reactor mounting) and illuminated by the sun in such a way that the reflections have the power to singe/burn items within the fenced area. Therefore, it was imperative that care is taken and a model of solar position, dish position and predicted reflections was created in order to determine the location of reflections (to ensure they are away from office windows) and the timeframe that the dish is in shadow. The resulting graphical user interface built in MATLAB can be seen in Figure 3.8 where the bright blue line on the left plot shows the position of the reflections. It is important to note that this challenge is unique to the densely populated university campus setting and for industrial installations, this challenge may be avoided.

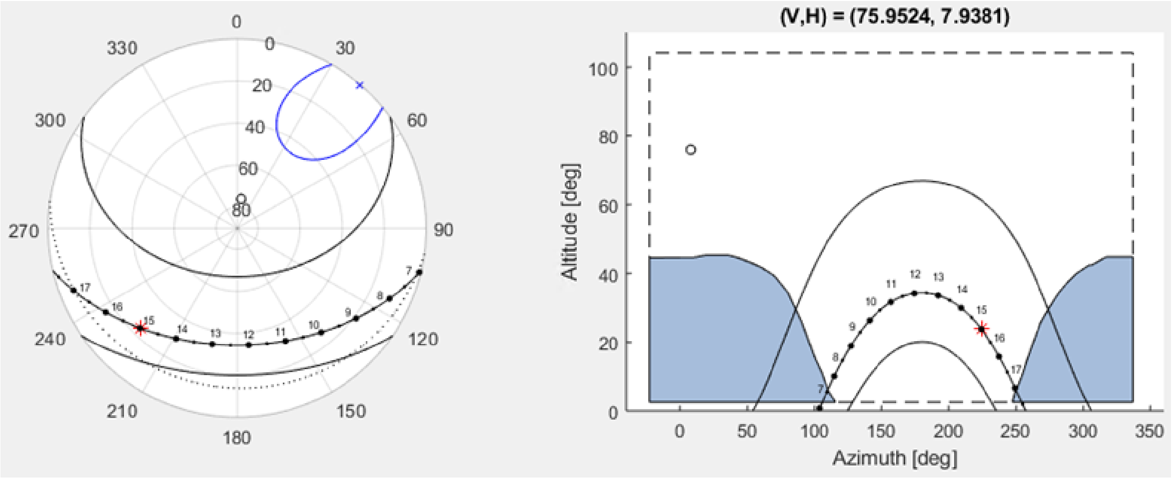

Figure 3.8: Graphical user interface of the solar position and reflection direction prediction script. The predicted solar trajectory over the chosen day is shown along with the winter/summer solstice solar trajectory. Predicted reflections based on the current solar position (red star) is shown as a blue line (x = center of reflections) on the left plot.

3.7 Public interface

In order to engage both the public and researchers in the field of solar fuels, an online public interface was hosted at https://solardish.epfl.ch/. This promotes dissemination of the project achievements to a wider audience than those with access to journal subscriptions. The control and monitoring LabVIEW script periodically sends results to a SQL database hosted at EPFL, and then the contents of the database are then visualised using Grafana “dashboard”, an open source data visualization web application. A screenshot of the public interface can be seen in Figure 3.9, where current and historical trends of production rates, system efficiencies, temperatures, pressures, currents and voltages are shown.

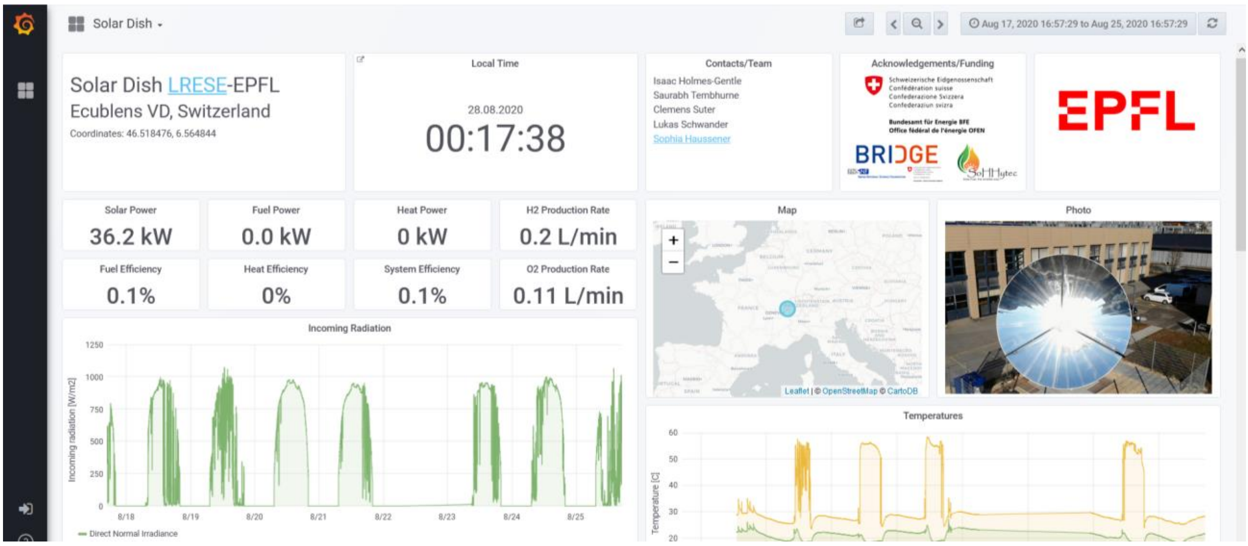

Solar Dish

Aug 17, 2020 16:57:29 to Aug 25, 2020 16:57:29

Solar Dish LRESE-EPFL
Ecublens VD, Switzerland
Coordinates: 46.518476, 6.564844

Local Time
28.08.2020
00:17:38

Contacts/Team
Isaac Holmes-Gentle
Saurabh Tembhurne
Clemens Suter
Lukas Schwander
Sophia Haussener

Acknowledgements/Funding
Schweizerische Eidgenossenschaft
Confédération suisse
Confederazione Svizzera
Confederaziun svizra
Bundesamt für Energie BFE
Office fédéral de l'énergie OFEN

Solar Power: 36.2 kW
Fuel Power: 0.0 kW
Heat Power: 0 kW
H2 Production Rate: 0.2 L/min
Fuel Efficiency: 0.1%
Heat Efficiency: 0%
System Efficiency: 0.1%
O2 Production Rate: 0.11 L/min

Figure 3.9. Snapshot of solar dish public interface allowing for an in-situ observation of the solar irradiation conditions, temperatures and pressures in the system, hydrogen and oxygen production rates, estimated system and device efficiencies, and current-voltage operating conditions.

4 Methodology

4.1 Experimental methodology

4.1.1 Optical characterization

Solar dish – The optical methodology developed in Ref. [16] was applied to determine the spatial distribution of the incident solar radiative flux. The radiative flux measurement system consisted of a water-cooled Lambertian target, a CCD camera and a radiative flux gage. Radiative flux measurements were performed at positions of the target ranging from $z = 5 – 15$ cm from the reference front edge of the receiver bracket, see scheme in Figure 4.1. By convention, $z > 0$ defines planes closer to the solar dish's apex, and $z < 0$ planes further away from the solar dish's apex.

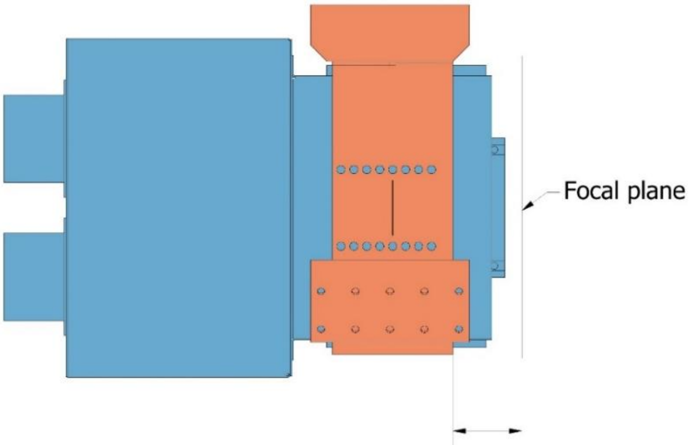

Figure 4.1. Scheme showing focal plan with respect to reference front edge of the receiver bracket ($z = 0$). The receiver bracket is indicated in red. The reactor is shown in blue.

The DNI was measured by a pyrheliometer (SPN1 sunshine pyranometer, Delta T Devices). Data were provided by the Solar Energy and Building Physics Laboratory of EPFL. The sensor is mounted on the roof of the ELG building. Thus, the distance between the sensor and the solar dish is approximately 50 m. The sensor is mounted horizontally and measures the global horizontal irradiance (GHI) as well as the diffuse horizontal irradiance (DHI). The DNI is then retrieved:

$$DNI = \frac{(GHI - DHI)}{\cos\theta} \tag{1}$$

where θ is the zenith angle of the sun, depending on the sun trajectory.

Mechanical stress – The weight difference between the reactor setup (80 kg) and the flux measurement setup (20 kg) was around 60 kg. Thus, we compensated the weight difference by additional weights, see Figure 3.7a.

Monte-Carlo ray-tracing simulations – The optical performance of the solar dish was evaluated using collision-based Monte Carlo ray-tracing simulations. The model was implemented in the open source program VEGAS written in Fortran 95 [19].

4.2 Modelling methodology

Alongside the experimental research into the integrated photo-electrochemical cell system, we have studied the generic system performance via a high fidelity simulation. The model parameters are taken to closely represent the real system, but permit the flexibility to vary key design parameters.

In order to investigate the fundamental dynamics of the system, only key components (photoabsorber, electrochemical parts, pump and piping) are selected from the complete generic system. This simplification means the dynamic behavior intrinsic to the proposed device can be studied whilst neglecting the extraneous downstream components, such as the liquid-gas separation and end user dependent gas processing steps. All the neglected components can be designed to meet the requirements imposed by the integrated device dynamics studied herein.

As the system considered here is thermally integrated, the concentrated solar irradiance and operating conditions will significantly impact the operating temperatures, and hence it is expected to exhibit a dynamic response to a far greater extent than for non-concentrating PV fields coupled to power electronics and a temperature controlled EC. As comprehensively reviewed by Carmo et al. [20], whilst there have been many time-dependent models of varying approaches developed for PEM ECs [21]–[26], there have been no dynamic models of thermally coupled photo-electrochemical devices using concentrated solar radiation. Therefore, this model will facilitate new insight into the expected dynamic phenomena, highlight the synergistic effect of the integration, and allow to assess the impact on the system performance and to discuss the consequences on the control strategy.

4.3 Model description

The modelled generic system is comprised of the following key components: 1) a solar parabolic dish, 2) a III-V material based triple-junction photovoltaic component, 3) a proton exchange membrane (PEM) based electrochemical component, and 4) auxiliary components such as a pump, piping and heat exchanger (HX) for heat recovery (assuming ideal effectiveness).

A more detailed description of the model is found in our published publication [48]: Holmes-Gentle et al., *Dynamic system modeling of thermally-integrated concentrated PV-electrolysis*, International Journal of Hydrogen Energy, 2021.

4.3.1 Photovolatic component

The photovoltaic model is comprised of 3 parts: an electrical model, a thermal model and a mass/momentum model. Firstly, for electrical model the triple junction PV cell is modelled as three single diode equivalent circuits (Eq. (2)) electrically coupled in series [27]. From the single cell electrical performance, the component's voltage and current can be calculated assuming homogenous PV temperature and solar flux distribution with $V_{PV} = N_{PV,s} \times V_{PV,cell}$ and $I_{PV} = N_{PV,p} \times I_{PV,cell}$ where $N_{PV,s}$ is the number of triple junction equivalent circuit in series to make a single 'string' and $N_{PV,p}$ is the number of 'strings' in parallel. The cell current I_i and voltage V_i relation of a single junction subcell i of the triple junction requires knowledge of the reverse saturation current, $I_{o,i}$, series resistance, $R_{s,i}$, elementary charge, q, ideality factor, n_i, and Boltzmann constant k_B. It is assumed that the photo-current $I_{L,i}$ is equal to the short circuit current $I_{sc,i}$ and that the shunt resistance $R_{sh,i}$ is large enough to neglect the final term. All junctions are assumed to be at the same temperature T_{PV}.

$$I_i = I_{L,i} - I_{o,i}\left(\exp\left(\frac{q\left(V_i + I_i R_{\mathrm{s,i}}\right)}{n_i\, k_B\, T_{PV}}\right) - 1\right) - \frac{V_i + I_i\, R_{\mathrm{s,i}}}{R_{sh,i}} \tag{2}$$

The short circuit current is assumed to be linearly proportional to the solar irradiance concentration, C. C is a multiple of standard 1 Sun conditions where 1 Sun is equal to 0.9 kW m^{-2} (AM1.5D). Temperature dependence of the short circuit current is approximated to be linear [28] within a defined temperature range where μ_{Isc} is a temperature dependent proportionality coefficient.

The diode reverse saturation current for junction *i* is a function of T_{PV}, bandgap $E_{g,i}$ and a number of constants κ_i, γ_i, n_i (Eq. (3)). The temperature dependence of the cell bandgap $E_{g,i}$ is commonly expressed as a function of T_{PV}, the bandgap at absolute zero E_g(0 K) and two material dependent properties α and σ as detailed by Varshni [29]. The bandgap of the top two layers are semiconductor alloys is calculated following Vurgaftman et al. [30].

$$I_{o,i} = A_{PV,cell}\, \kappa_i\, T_{PV}{}^{(3+\gamma_i/2)} \exp\left(\frac{-E_{g,i}}{n_i k_B T_{PV}}\right) \tag{3}$$

Secondly, the thermal model considers the heat removed from the PV’s heat sink by the cooling water. A 0-dimensional thermal resistance model is employed as shown in Eq. (4) where the PV component, the heat sink (HS) and the inlet/outlet cooling water (CW) are each defined by a temperature. Here, $H_{CW,inlet/outlet}$ is the inlet/outlet enthalpy of the cooling water, $P_{solar,PV}$ is the total solar input power to the component, f_{abs} is the fraction of light incident which is absorbed and the subscript "*amb*" denotes the ambient surroundings. Accumulation of heat is only considered in the heat sink, as it has a significant thermal mass C_{HS}.

$$\begin{aligned} 0 &= f_{abs} P_{solar,PV} - V_{PV} I_{PV} - Q_{PV\to HS} \\ C_{HS} \frac{dT_{HS}}{dt} &= Q_{PV\to HS} - Q_{HS\to CW} - Q_{HS\to amb} \\ 0 &= H_{CW,inlet} - H_{CW,outlet} + Q_{HS\to CW} \end{aligned} \tag{4}$$

Heat transfer between the PV and the heat sink is due to thermal conduction: $Q_{PV\to HS} = U_{PV\to HS} A_{PV}(T_{PV} - T_{HS})$. The overall heat transfer coefficient $U_{PV\to HS}$ is considered constant over the temperature range and is calculated according to Theristis et al. [31]. The overall heat transfer coefficient for heat sink to ambient surroundings $U_{PV\to amb}$ was also assumed constant neglecting wind speed, humidity effects due to dominance of the convective heat transfer to the cooling water.

For the heat transfer due to forced convection through the micro-channelled heat sink, a geometry is estimated and the NTU (Number of Transfer Units) method was used to calculate the heat transferred taking into account the heat exchanger fin efficiency. As the overall heat transfer coefficient $U_{HS\to CW}$ is dominated by the interfacial convective transport, it can be calculated from Nusselt number correlations for fully developed laminar flow rectangular channels [32].

Finally, the mass and momentum balances yield the outlet mass flowrate and pressure drop. Within the operating conditions considered (<100 °C), water can be considered incompressible and therefore $\dot{m}_{CW,inlet} = \dot{m}_{CW,outlet}$. The pressure drop is given by the Darcy–Weisbach equation (Eq. 5), where ρ is the fluid density and the friction factor f_D can be computed from empirical correlations for rectangular channels [32]. The mean velocity v within the channel of cross-sectional area $A_{HS,cross}$ and length L is calculated with $v = \dot{m}/\rho\, A_{HS,cross}$. D_h is the hydraulic diameter of the channel.

$$\Delta p = f_D \, \frac{L\rho v^2}{2\, D_h} \tag{5}$$

4.3.2 Electrochemical component

The electrochemical performance of the PEM EC is coupled with a mass conservation model in order to simulate the dynamic behavior. The voltage vs. current dynamic response of a PEM EC is commonly assumed to be instantaneous [33] and therefore will be modelled with a time-invariant model. Consequently, any dynamics observed in the electrical variables will result from time-variant parameters (e.g. the species concentration, temperature, pressure etc.).

Neglecting the concentration overpotential due to mass transfer effects (as the typical current densities of PEM ECs are sufficiently below the limiting current density [21], [34]) the cell potential can be expressed as $V_{EC,cell} = E_{redox} + \eta_{kinetic} + \eta_{ohmic}$. The (reversible) electrochemical redox potential of water splitting E_{redox} is calculated from the Nernst equation taking into account the temperature dependence of the standard electrode potential. The kinetic overpotential $\eta_{kinetic}$ is defined as the sum of the oxygen evolution reaction and hydrogen evolution reaction overpotentials, each of which can be related to the current via the Tafel equation (shown in Eq. (6)). This simplification of the Butler-Volmer equation is valid as the normal operating range of PEM ECs means that low currents are inadvisable (due H_2 cross-over). The temperature dependence of the anodic and cathodic exchange current density can be modelled using an Arrhenius type equation [13], [21], [35]where E_a is the activation energy and $i_{\circ,ref}$ is the exchange current density at a reference temperature T_{ref}.

$$\eta_{kinetic} = \frac{R\, T_{EC}}{\alpha_a\, n_e\, F} \ln\left(\frac{i_{EC,cell}}{i_{\circ,a}}\right) + \frac{R\, T_{EC}}{\alpha_c\, n_e\, F} \ln\left(\frac{i_{EC,cell}}{i_{\circ,c}}\right) \tag{6}$$

The ohmic losses are assumed to come only from the electrical resistance of the membrane. The temperature dependence of the membrane conductivity σ_m is given by an empirical correlation [36] shown in Eq. (7) where T_{EC} is EC temperature and λ_m is the degree of humidification.

$$\sigma_m = (0.00514\, \lambda_m - 0.00326) \exp\left(1268 \left(\frac{1}{303} - \frac{1}{T_{EC}}\right)\right) \tag{7}$$

The thermal model of the electrochemical component is given by Eq. (8) where it is assumed the thermal mass C_{EC} is constant over the operational temperature range. The overall heat generated by the electrolysis Q_{gen} is due to the kinetic and ohmic losses being greater than the thermoneutral potential E_{th}. The heat transferred to the fluid in the anodic and cathodic chambers is estimated from an empirical data where the driving temperature difference for heat transfer to the fluid is defined as the difference between the (uniform) cathode or anode chamber fluid temperature and the EC temperature.

$$\begin{gathered} C_{EC} \frac{dT_{EC}}{dt} = Q_{gen} - Q_{fluid,a} - Q_{fluid,c} \\ Q_{gen} = A_{EC,cell}\, i_{EC,cell}\, N_{EC,s} \left(V_{EC,cell} - E_{th}\right) \\ Q_{fluid,a/c} = (UA)_{fluid,a/c} \left(T_{EC} - T_{fluid,out,a/c}\right) \end{gathered} \tag{8}$$

The mass and energy conservation model was applied to the anodic and cathodic chamber separately. For all components i, a component mass balance can be specified in Eq. (9) where M_i, $x_{\frac{inlet}{outlet},i}$, $\dot{m}_{inlet/outlet}$, $M_{w,i}$ and v_i are the accumulated mass of i, mass fraction of i, total mass flowrate, molecular weight of i, stoichiometry coefficient of component i, respectively. R_{rxn} is the molar reaction rate and is calculated using Faraday's law of electrolysis. The energy balance over the EC chamber is given in Eq. (10). Empirical equations of state can then be used to calculate the volume assuming ideal mixing.

$$\frac{dM_i}{dt} = x_{inlet,i} m_{inlet} - x_{outlet,i} m_{outlet} + M_{w,i} v_i R_{rxn} \text{ for all components } i \tag{9}$$

$$\frac{dE_{holdup}}{dt} = h_{inlet} m_{inlet} - h_{outlet} m_{outlet} + Q_{fluid} \tag{10}$$

4.3.3 Auxiliary components

Key auxiliary component such as the solar dish, the pump and piping have been included in the model. The total amount of solar power transferred to the CPV, $Q_{solar \to CPV}$, is calculated by Eq. (11), where A_{dish} is the area of light collected by the dish. The optical efficiency η_{opt} can be decomposed into the multiplication of the solar weighted reflectance ρ_s, the intercept factor γ_{dish} and a dish cleanliness factor η_{clean} which is assumed to be equal to 1.

$$Q_{solar \to CPV} = \eta_{opt} A_{dish} \mathrm{DNI} \quad \text{ where } \eta_{\mathrm{opt}} = \rho_s \gamma_{dish}\, \eta_{clean} \tag{11}$$

The pumping power is calculated from Eq. (12), where η_{pump} is the pump efficiency and is assumed constant. F_{pump} is the volumetric flowrate and Δp_{sys} is the total pressure drop over the system (i.e. piping, PV and EC).

$$P_{pump} = \frac{\Delta p_{sys}\, F_{pump}}{\eta_{pump}} \tag{12}$$

4.3.4 Efficiency definitions

The overall system solar-to-hydrogen efficiency is defined by Eq. (13) using the Gibbs free energy of water electrolysis (ΔG_{rxn} = 237.1 J mol^{-1}). The thermal system efficiency is defined by Eq. (14) where Q_{HX} is the useful thermal power extracted from the heat exchanger (HX). The total input solar power P_{solar} is defined based on the DNI ($P_{solar} = DNI \times \pi {D_{dish}}^2/4$). In the model study, only the pumping power P_{pump} is considered (i.e. P_{other} = 0). The system efficiency of co-generation of heat and fuel is then defined as $\eta_{sys} = \eta_{H2} + \eta_{thermal}$.

$$\eta_{H2} = \frac{R_{rxn} \Delta G_{rxn}}{P_{solar} + P_{pump} + P_{other}} \tag{13}$$

$$\eta_{thermal} = \frac{Q_{HX}}{P_{solar} + P_{pump} + P_{other}} \tag{14}$$

The component electrical efficiencies for the PV component and the PEM electrochemical component (based on ΔG_{rxn}) are typically defined as Eq. (15), where $P_{solar,PV}$ is the total power of solar radiation incidence on the solar cells. Here, V_{PV}^{mpp} and I_{PV}^{mpp} are the voltage and current at the Maximum Power Point (MPP).

$$\eta_{PV}^{mpp} = \frac{V_{PV}^{mpp} I_{PV}^{mpp}}{P_{solar,PV}} \qquad \eta_{EC} = \frac{\eta_F E_{redox}}{V_{EC,cell}} \tag{15}$$

4.4 Model parameters

This model is based on a dataset taken from literature, manufacturer datasheets and estimated from experimental data, typical values or empirical correlations. The key parameters are given in Table 1 of our modelling paper [48] where the dish considered is power-matched to integrated reactor (i.e. smaller diameter) and a higher intercept factor. The nominal hydrogen production power of the modelled system is approximately ~2 kW (based on enthalpy) for a DNI = 1000 W m^{-2} which corresponds to an input solar power of ~8.5 kW.

The numerical solution of the mixed differential-algebraic model was accomplished with gPROMS ModelBuilder 5.1.1. The standard solver (DAEBDF) based on Backward Differentiation Formulas was used. The inbuilt PhysProp package was used for all thermodynamic calculations not explicitly specified in the following section.

5 Results

5.1 Process simulation results

It is important to note that these results are for the generic system in order to show optimized system performance and the realizable potential of this technology. Therefore, the general behavior will be comparable, but the predicted efficiencies are higher due to improved power matching between solar parabolic dish and the integrated reactor.

A more detailed description of the results is found in our published publication [48]: Holmes-Gentle et al., *Dynamic system modeling of thermally-integrated concentrated PV-electrolysis*, International Journal of Hydrogen Energy, 2021. The figures in section 5.1 are also reproduced from this paper.

5.1.1 Steady-state sensitivity analysis

The position of the operating point of the integrated device is heavily dependent on the operating temperature of both photovoltaic (PV) and electrochemical (EC) devices. As a first assumption, the PV and EC electrical models are solved with $T_{PV} = T_{EC}$ for various temperatures, solar irradiance, and number of EC cells in series. This is shown in Figure 5.1a, highlighting the operating point (intersection of PV and EC curves). For all cases simulated, the increase in temperature reduces the operating voltage. For the operating current, two contrasting behaviors are observed dependent on the relative position of the operating point to the Temperature Stationary Point (TSP) of the PV curve. Here, we defined the TSP as the point where $dI_{PV}/dT_{PV} = 0$ and is shown in Figure 5.1b where the TSP is found at lower voltages/higher currents than the maximum power point (MPP). For operating voltages (V_{op}) lower than TSP voltage (V_{TSP}), the current increases moderately as the short circuit current increases with temperature. Conversely, for $V_{op} > V_{TSP}$ the current decreases significantly as the open circuit voltage decreases. This crude analysis ($T_{PV} = T_{EC}$) succinctly demonstrates the necessity for an accurate thermal model due to the sensitivity of the system performance to temperature.

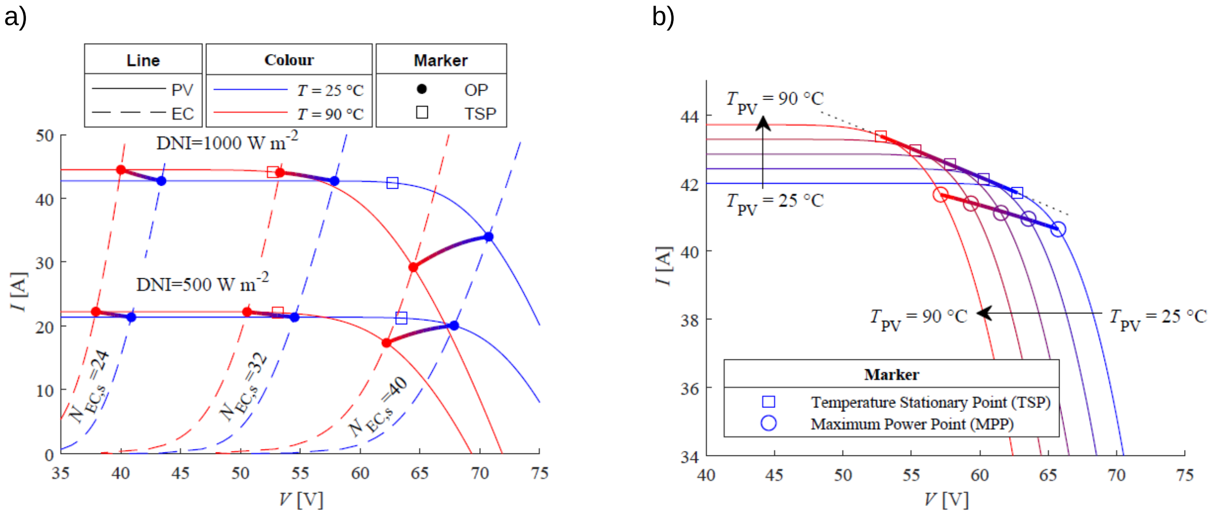

Figure 5.1. a) Steady-state electrical model (PV, EC) for two hypothetically equal operating temperatures denoted as $T = T_{EC} = T_{PV}$ highlighting the position of the temperature stationary point (TSP). The continuum of operating points (OP) at intermediate temperatures is displayed as a line with linear colour gradient. b) The current-voltage relationship of the PV component highlighting the position of the maximum power point (MPP) and the temperature stationary point (TSP) is shown for T_{PV} between 25 and 90 °C.

Following this, the complete dynamic model was solved in order to determine the PV and EC steady state temperatures for various conditions through simulation over adequately long timescales (i.e.

~1000s of seconds). As expected, the operating temperatures increase with decreasing flowrate and at lower flowrates (<2 l/min) a stronger rise in temperature is observed (see in Figure 5.2b for DNI = 1000 W/m^2). This strong increase in temperature potentially poses a control challenge which will be subsequently explored, as a small perturbation in flowrate could lead to a large rise in operating temperature. Furthermore, Figure 5.2b shows that the temperature difference between PV and EC is also a function of water flowrate (i.e. difference increasing with increasing flow rate), due to the changing effectiveness of the heat transfer to the water in the PV heat sink.

For F_{pump} varying between 1 - 10 l/min and $N_{EC,s}$ between 28 - 40 (see Figure 5.2a), the maximum efficiency is in the range of ~16-21% and significantly contrasting behaviors at different coupling ratios (i.e. $N_{EC,s}/N_{PV,s}$) is observed. For smaller $N_{EC,s}$ (e.g. $N_{EC,s} = 28, 30, 32$), the maximum efficiency is obtained at the lowest permissible flowrates and therefore highest operating temperatures. For higher coupling ratios (e.g. $N_{EC,s} = 34, 36, 38, 40$) when the operating point is at higher voltages than the maximum power point of the PV, the highest efficiencies are conversely found at higher flowrates and therefore lower T_{PV}. This behaviour can be explained by the previous discussion of Figure 5.1a, where the effect of the increase in short circuit current dominates over the decrease in open circuit voltage for lower coupling ratios and vice-versa for higher coupling ratios. For larger flow rates (5-10 l/min), a decrease in efficiency is again observed, resulting from the increase in the pumping power, adversely affecting the efficiency.

Additionally, Figure 5.2a shows that there is a significant decrease in η_{H2} at higher coupling ratios for water flowrates <2 l/min. This leads to a larger fraction of solar irradiance that is converted to heat and the significant resistance to heat transfer leads to an increase in PV temperature, which can further shift the operating point. This positive feedback loop accentuates the control challenge at flowrates <2 l/min and conceptually could lead to thermal runaway type situation which is investigated further in the following discussion.

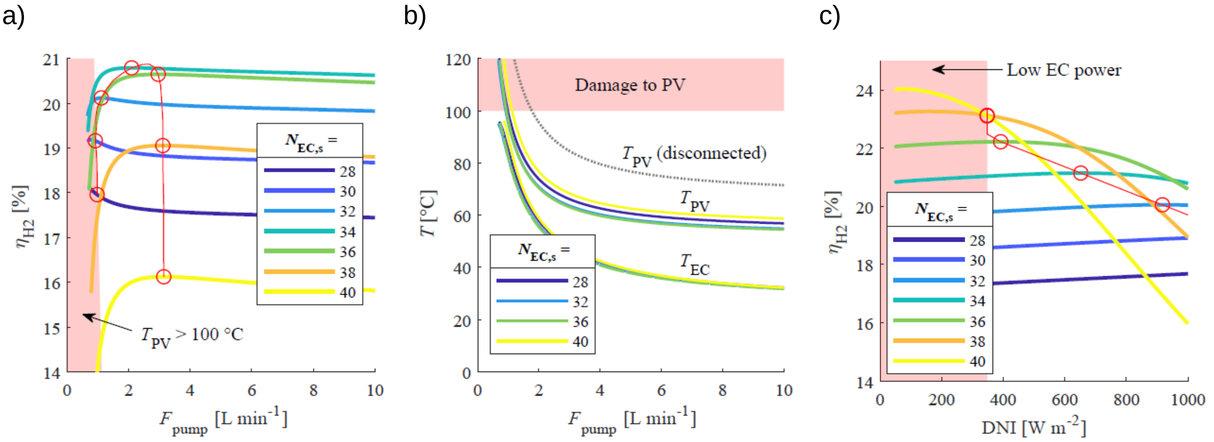

Figure 5.2. a) Hydrogen efficiency vs. water flowrate for various $N_{EC,s}$. b) The steady-state system temperatures (PV and EC) vs. water flowrate for various $N_{EC,s}$. Additionally, the steady-state PV temperature resulting from electrical disconnection is shown and is not dependent on $N_{EC,s}$. c) Hydrogen efficiency vs. DNI for various $N_{EC,s}$ where water flowrate = 2 l/min. In both a) and c) the red line denotes the respective operating conditions which maximize the efficiency for each $N_{EC,s}$ within operational limits (i.e. $T_{PV} < 100$ °C and $I_{EC} > 15$ A).

The sensitivity of the fuel conversion efficiency to the DNI is shown in Figure 5.2c and the observed behavior can be explained by the logarithmic dependence of the open circuit voltage and linear dependence of the short circuit current with light intensity (which shifts the maximum power point voltage) while also considering a temperature effect (as the operating temperatures are dependent on irradiance). This, in turn, affects the voltage–current coupling of the PV and EC which impacts the system efficiency accordingly (dependent on the operating point relative to the TSP). As DNI increases, the TSP shifts to lower potentials while the operating voltage moves to larger potentials (as current increases) whilst also considering the increased operating temperatures which reduces the TSP significantly and the operating point to a lesser extent. The resulting general behavior is that increasing DNI leads to a better coupling efficiency when $V_{op} < V_{TSP}$ (see $N_{EC,s} = 28$ in Figure 5.2c) up until $V_{op} > V_{TSP}$ where an increasing DNI leads to a worse coupling efficiency (see $N_{EC,s} = 40$ in Figure 5.2c).

5.1.2 System dynamics

Various instantaneous step changes in DNI and F_{pump} are made in order to investigate the system dynamics. The observed dynamic electrical performance of the CPV and the EC originates from the changes in their operating temperatures and pressures as both electrical models respond instantaneously. We considered the major disturbance to be DNI and major controlled variable to be the water flowrate.

It was found that the response time of T_{PV} is about 2-3 times as fast compared to T_{EC} for a step change in water flowrate. This leads to an interesting dynamical effect on the electrical operating point of the integrated reactor. Furthermore, when $V_{op} < V_{TSP}$ increases in PV temperature lead to an increase in the PV short circuit current increase and vice-versa, leading to non-linear behavior dependent on PV to EC ratio, temperature and DNI etc.

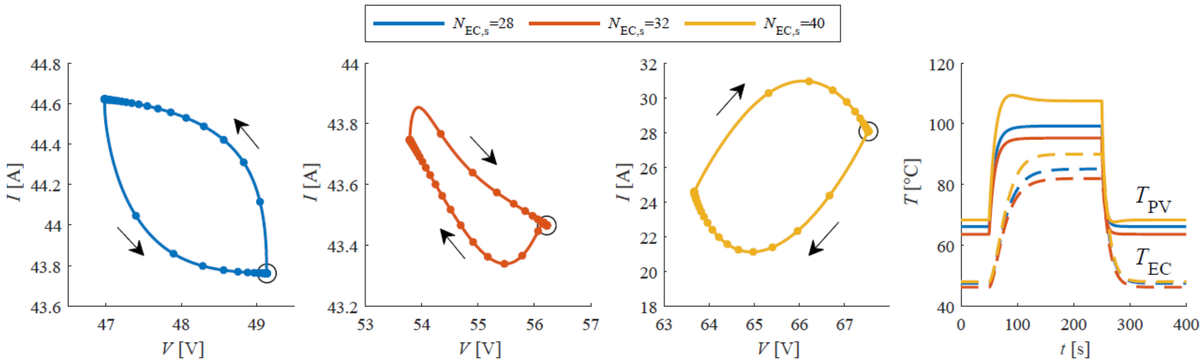

Figure 5.3. The trajectory of the operating point for varying $N_{EC,s}$ for a step change in F_{pump} (3 → 1 at 50 s and 1 → 3 L min^{-1} at 250 s) and DNI = 1000 W m^{-2} is shown in a), b) and c). Each marker is spaced at 5 seconds intervals and the arrows show direction of trajectory from the starting point (t = 0 s) denoted by a black circle. The corresponding PV and EC temperature changes are shown in d).

To visualize the dynamic phenomena, the trajectory of the operating point (in the current-voltage domain) as a function of time for step changes in F_{pump} and DNI is investigated for varying $N_{EC,s}$. Figure 5.3 demonstrates the hysteresis in operating point trajectory due to the contrasting time scales between the temperature response of the PV and the EC (specifically, the PV temperature responds faster). Additionally, Figure 5.3 shows a PV temperature overshoot for $N_{EC,s} = 40$ as the position of the electrical coupling (i.e. right of MPP) makes it particularly sensitive to temperature changes. Shown in Figure 5.3c for the step decrease in F_{pump}, the operating current passes through a minimum before increasing to the steady-state value caused by the delayed temperature increase in T_{EC}. As the electric power extracted increases, the PV heat transfer requirements decrease leading to the ultimately lower T_{PV}. This demonstrates the highly coupled nature of operating conditions, temperatures, and power. Correspondingly, the system response to step changes in DNI can be seen in Figure 5.4 where the initial instantaneous change in operating point is caused by the dependence of the PV short circuit current on the solar concentration and which is then followed by a response comparable to Figure 5.3 caused by the thermal dynamics.

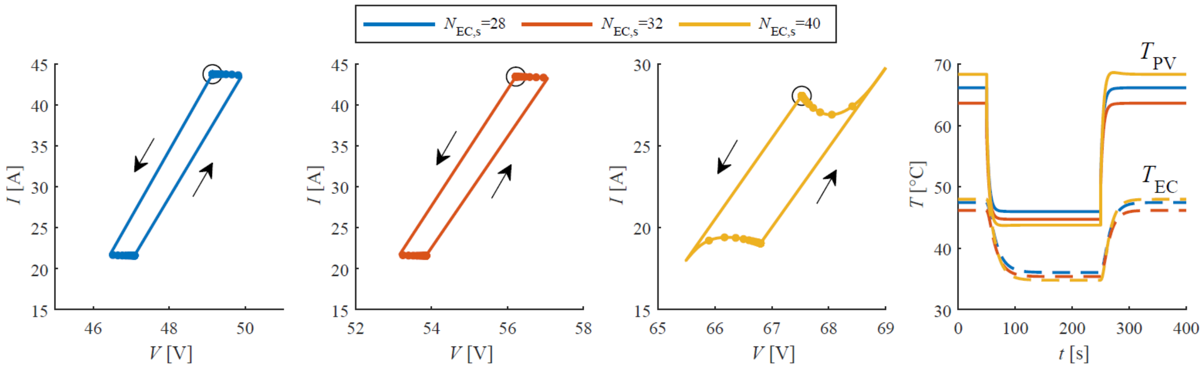

Figure 5.4. The trajectory of the operating point for varying $N_{EC,s}$ for a step change in DNI (1000 → 500 at 50 s and 500 → 1000 W m^{-2} at 250 s) and F_{pump} = 3 L min^{-1} is shown in a), b) and c). Each marker is spaced at 10 seconds intervals and the arrows show direction of trajectory from the starting point (*t* = 0 s) denoted by a black circle. The corresponding PV and EC temperature changes are shown in d).

This analysis shows that dynamic effects are observed, specifically operating temperatures stabilize within 1-2 minutes for changes in DNI and water flowrate, which is comparable to the timescales of typical intermittent irradiance conditions. This highlights the control challenge of stable operation under cloudy conditions.

However, the system is very responsive to changes in DNI, as seen in Figure 5.4 indicating that intermittent conditions will not cause a significant reduction in H_2 efficiency. It is important to note that in this work a comparatively small electrochemical component (nominal power ~3 kW) was modelled and a larger system would have slower thermal dynamics due to the higher thermal inertia of the components. This could potentially represent a greater control challenge but the close coupling of the EC and the solar dish CPV system limits the size of the EC due to constraints in the feasible solar parabolic dish areas and the diffuse nature of solar irradiance.

5.2 Optical characterization of solar dish

Figure 5.5 shows the peak concentration as well as the mean concentration averaged over the entire flux-target (area of 275 mm x 275 mm) as a function of the target position. The focal plane was assumed for the highest mean concentration on the target, yielding z = 100 mm. For z < 95 mm and z > 100 mm, the peak and mean concentration decrease with increasing distance from the focal plane (z = 100 mm). The intercepted solar radiation at the focal plane is 29.6 kW$_{th}$ for a DNI of 1000 W/m^2.

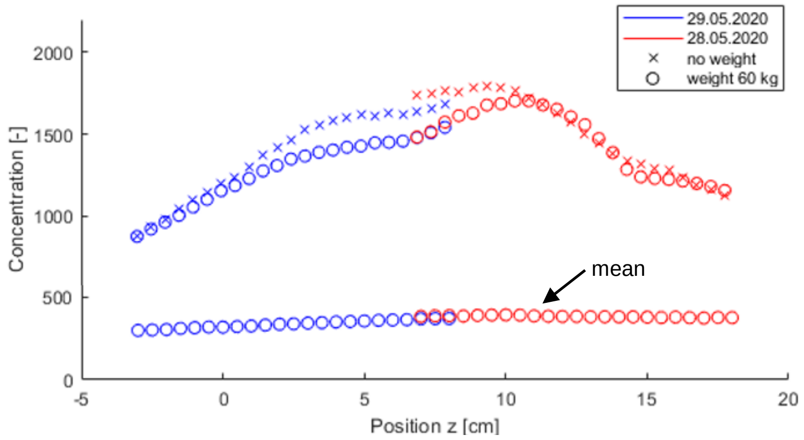

Figure 5.5. Peak concentration (without and with 60 kg external weight) and mean concentration averaged over 275 x 275 mm^2 target (for weightless case) as a function of the target position. Target position is distance from the reference front edge of the dish's receiver bracket.

5.3 Integrated system experiments

The best result of a multi-day test (4 days) in summer of the integrated system are discussed here. As shown in Figure 5.6, the four days over which the test occurs had varying meteorological conditions (i.e. intermittent dense cloud cover on 19/08/2020, clear blue skies 20/08/2020 and light hazy cloud cover in the morning of 24/08/2020).

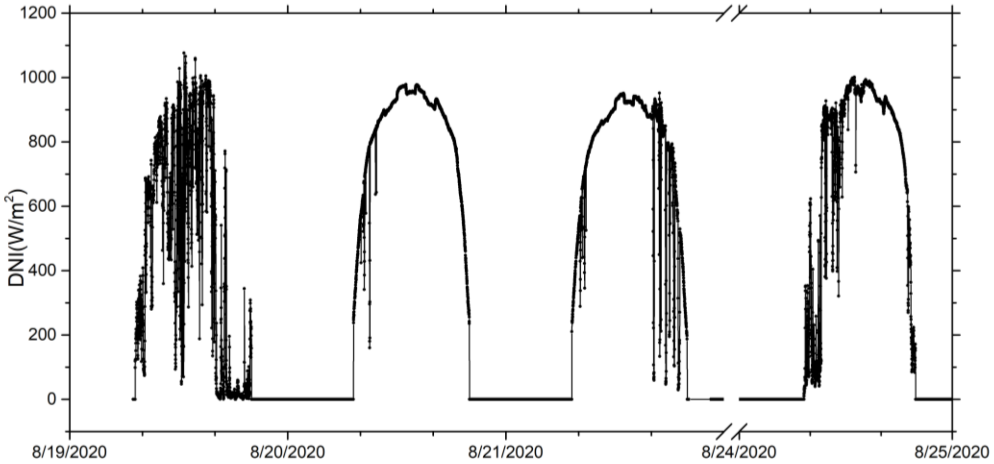

Figure 5.6. Direct normal irradiance over 4 days during integrated system testing.

The volumetric production rates of H_2 and O_2 were calculated from the operating current assuming a faradaic efficiency of unity. The production rate profiles follow the irradiation profile. The temperature of the inlet and outlet of the process were monitored as well, with the sensors positioned in the tunnel to give an accurate measure of the amount of heat extractable from the system. The EC outlet temperature is typically ~70ºC meaning there is significant heat lost in the pipes between the reactor and the tunnel, which could be reduced by improving piping insulation. The typical operating (absolute) pressures in the anodic side is ~3.5 bar, the cathodic side ~29 bar and in the H_2 storage tank is 1-31 bars. For the best day (August 8, 2020), we measured an average DNI of 932 W/m^2, 7.77 hours of continuous operation, an average system solar-to-hydrogen efficiency of 6.0% (based on Gibbs energy), an average system solar-to-heat efficiency of 39.1%, an average system solar-to-hydrogen&heat efficiency of 45.1%, an average diagnostic solar-to-hydrogen device efficiency of 21.1%, and produced 108.8 kWh_{th} thermal energy.

6 Summary and Conclusions

In this project, we have designed, implemented, characterized and operated a scalable thermally integrated PEC system at the ~15 kW power scale that is able to produce up to ~0.5 kg of hydrogen during a nice, sunny day. The scaled design has been based on our laboratory scale demonstration [5] with the corresponding extension to system level, i.e. integrating it with a solar concentrator, pump, in-house oxygen-water and hydrogen-water separators, and compressor. Characterization methods and in-situ performance characteristics have been developed and recorded to provide access to system performance and to identify the most limiting and critical components.

The recorded data of the overall system performance is available to the public via a dedicated, developed public interface (https://solardish.epfl.ch/). CIPEC device-level efficiency of 21.1% was measured, and a co-generation system level solar-to-hydrogen&heat efficiency of 45.1% was recorded. These are very encouraging numbers which have motivated us to establish a startup company (https://www.sohhytec.com/) with which we will explore further scalability of the system to the 100 kW scale, its integration with industrial customers (such as steel manufacturer), and its commercialization as a solar fuel facility.

A multi-day experimental campaign (4 days) was conducted and showed robust and stable operation. Additional, multi-day campaigns have been conducted in winter conditions as well, confirming robust and stable operation year round. We have now at our finger tips a solar fuels plant or system, which is an excellent experimental platform that is automated and will be exploited in the coming years to further collect data of this solar reactor (and/or improved and optimized reactor designs) and the overall system to better understand and quantify long term performance as well as to help in defining benchmarks and experimental procedures for reproducible performance quantification in realistic solar environments.

The design and operation of the system has been supported by a transient multi-physical system model The model predicts interesting coupling phenomena in the system due to the thermal integration and the different thermal inertia of the various components. The solar plant and the model have then been used to explore operational and product flexibilization approaches, considering possible controlling approaches and co-generation schemes (simultaneous production of fuel plus heat and electricity production). These simulations show that the capacity factor can be significantly increased when grid-electricity can be used to support the operation (in a hybrid sun-grid mode). Additionally, the co-generation product portfolio has been demonstrated for fuel and heat, but an extension for the simultaneous production of fuel, heat and electricity is also predicted by the model. Dedicated experimental campaigns will specifically explore the sun-grid hybrid operational mode (as a function of the solar irradiation condition, or for night-time operation) and will quantify the co-generation potential in the solar transient environment.

The chemistry flexibilization has been assessed only at the laboratory scale and for the photo-electrochemical reduction of CO_2 to CO. Specifically, we have used the lab-scale device (see Figure 2.1a) and adapted the cathodic side for a feed of humidified CO_2, and incorporated a hydroxyl ion conducting solid electrolyte and a silver based catalyst. The anodic side was not changed. This activity was conducted in collaboration of Prof. Janaky's group at the University of Szeged in Hungary [46], [47] who provided us with the silver catalyst in a gas diffusion electrode. The results of a first run in our high-flux solar simulator are shown in Figure 6.1. Our CIPEC device was operated at an irradiation concentration of 147. The resulting Faradaic efficiency for CO was 50% (the reminder was hydrogen production). This first demonstration resulted in a solar-to-CO efficiency of 1.25%. While this performance is not yet satisfactory, it shows the first time the utilization of concentrated irradiation in a photo-electrochemical CO_2 reduction device with a reasonable selectivity and efficiency. This successful demonstration also illustrates that the same design approaches are feasible for the photo-electrochemical CO_2 reaction and that there is a possibility for a relatively straight forward translation of this device-scale demonstration into a larger scale system demonstration.

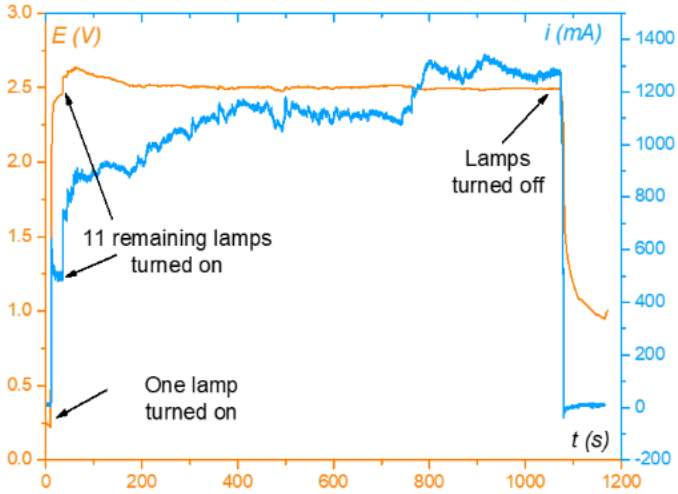

Figure 6.1. Potential (left *y*-axis) and current (right *y*-axis) as a function of operational time of our laboratory-scale CIPEC device utilized for CO_2 reduction instead of water splitting.

7 Project publications

Papers:

1. Holmes-Gentle, Tembhurne, Suter, Haussener, *Dynamic system modeling of thermally-integrated concentrated PV-electrolysis*, International Journal of Hydrogen Energy, 2021.
2. Holmes-Gentle, Tembhurne, Suter, Haussener, *Control strategies for thermally-integrated concentrated PV-electrolysis,* in preparation, 2021.
3. Suter, Tembhurne, Holmes-Gentle, Haussener, *Optical characterization of EPFL's 38.5 kW$_{th}$ solar dish*, in preparation, 2021.
4. Tembhurne, Holmes-Gentle, Clemens, Haussener, *Scaled Solar Hydrogen Production System Using Concentrated Integrated Photo-Electrochemical Device*, in preparation, 2021.

Public browser-based interface:

1. Public browser-based interface for instantaneous observation of system activity and performance: https://solardish.epfl.ch/

Invited and contributed conference presentations or peer reviewed conference papers (selection):

1. Haussener, *Solar fuel processing: Research, technology development, and scaling.* Invited oral presentation at: AIChE annual meeting, online, 2020.
2. Holmes-Gentle, Tembhurne, Suter, Haussener, *Dynamic process simulation and control of a high performance thermally-integrated concentrator photovoltaic and electrolysis co-generation device*. Oral presentation at: AIChE annual meeting, online, 2020.
3. Tembhurne, Holmes-Gentle, Suter, Haussener, *Modelling, experimentation and scaling of solar hydrogen generation devices.* Invited oral presentation at: PECSys workshop, online, 2020.
4. Haussener, *Technology Development and Scale-up of Solar Fuel Devices - Our journey*. Invited oral presentation at: International solar Fuels Forum, online, 2020.
5. Tembhurne, Holmes-Gentle, Suter, Haussener, *Scaled Photo-Electrochemical System for Solar Hydrogen Production utilizing Concentrated Irradiation*. Oral presentation at SolarPACES, online, 2020.
6. Suter, Tembhurne, Holmes-Gentle, Haussener, *Optical characterization of a solar concentrating dish system up to 1000 suns for solar fuel production*. Conference paper, Eurotherm2020 (postponed to 2021 due to COVID 19).
7. Holmes-Gentle, Tembhurne, Suter, Haussener, *Dynamic process simulation of a kW scale concentrated solar hydrogen producing device*. Presented at: NanoGe Fall meeting, Berlin, 2019.
8. Haussener, *Solar Fuel Generation: From Laboratory Demonstrations to Technology Development*. Invited oral presentation at: CHAINS, Veldhoven, 2019.

9. Haussener, *Modelling, design and thermal synergies in photo-electrochemical fuel processing devices.* Invited oral presentation at: Nature Solar Fuels Conference, Wuhan, 2019.

Student projects:

1. Master project: Morisseau, *Optical analysis of the EPFL solar parabolic dish*, 2020.
2. Semester project: Yu, *Optical characterization of solar concentrators using UAV: Review and novel approaches*, 2020.
3. Bachelor project: Schretter, *Photo-electrochemical fuel generation device operating under concentrated radiation*, 2020.

8 References

[1] N. Lewis and D. Nocera, “Powering the planet: chemical challenges in solar energy utilization,” *Proc. Natl. Acad. Sci. U. S. A.*, vol. 103, pp. 15729–15735, 2006.

[2] M. A. Modestino and S. Haussener, “An Integrated Device View on Photo-Electrochemical Solar-Hydrogen Generation,” *Annu. Rev. Chem. Biomol. Eng.*, vol. 6, 2015.

[3] A. Fujishima and K. Honda, “Electrochemical Photolysis of Water at a Semiconductor Electrode,” *Nature*, vol. 238, no. 5358, pp. 37–38, 1972.

[4] J. W. Ager, M. R. Shaner, K. A. Walczak, I. D. Sharp, and S. Ardo, “Experimental demonstrations of spontaneous, solar-driven photoelectrochemical water splitting,” *Energy Environ. Sci.*, vol. 8, no. 10, pp. 2811–2824, 2015.

[5] S. Tembhurne, F. Nandjou, and S. Haussener, “A thermally synergistic photo-electrochemical hydrogen generator operating under concentrated solar irradiation,” *Nat. Energy*, vol. 4, no. 5, pp. 399–407, 2019.

[6] T. J. Jacobsson, V. Fjällström, M. Edoff, and T. Edvinsson, “Sustainable solar hydrogen production: from photoelectrochemical cells to PV-electrolyzers and back again,” *Energy Environ. Sci.*, vol. 7, no. 7, pp. 2056–2070, 2014.

[7] M. G. Walter *et al.*, “Solar Water Splitting Cells,” *Chem. Rev.*, vol. 110, p. 6446-6473, 2010.

[8] M. Dumortier, S. Tembhurne, and S. Haussener, “Holistic design guidelines for solar hydrogen production by photo-electrochemical routes,” *Energy Environ. Sci.*, vol. 8, no. 12, 2015.

[9] M. R. Shaner, H. A. Atwater, N. S. Lewis, and E. W. McFarland, “A comparative technoeconomic analysis of renewable hydrogen production using solar energy,” *Energy Environ. Sci.*, vol. 9, no. 7, pp. 2354–2371, 2016.

[10] Zhai P. *et al.*, “Net primary energy balance of a solar-driven photo-electrochemical water-splitting device,” *Energy Environ. Sci.*, vol. 6, pp. 2380–2389, 2013.

[11] Dumortier M and S. Haussener, “Design guidelines for concentrated photo-electrochemical water splitting devices based on energy and greenhouse gas yield ratios,” *Energy Environ. Sci.*, vol. 8, pp. 3069–3082, 2015.

[12] R. Sathre *et al.*, “Life-cycle net energy assessment of large-scale hydrogen production via photoelectrochemical water splitting,” *Energy Environ. Sci.*, vol. 7, no. 10, pp. 3264–3278, 2014.

[13] S. Tembhurne and S. Haussener, “Integrated Photo-Electrochemical Solar Fuel Generators under Concentrated Irradiation - Part I: 2-D Non-Isothermal Multiphysics Modelling,” *J. Electrochem. Soc.*, vol. 163, no. 10, pp. H988–H998, 2016.

[14] S. Tembhurne and S. Haussener, “Integrated photo-electrochemical solar fuel generators under concentrated irradiation II. Thermal management a crucial design consideration,” *J. Electrochem. Soc.*, vol. 163, no. 10, 2016.

[15] G. Levêque, R. Bader, W. Lipiński, and S. Haussener, “Experimental and numerical characterization of a new 45 kW<inf>el</inf>multisource high-flux solar simulator,” *Opt. Express*, vol. 24, no. 22, 2016.

[16] M. Schubnell, J. Keller, and A. Imhof, “Flux density distribution in the focal region of a solar concentrator system,” *J. Sol. Energy Eng. Trans. ASME*, vol. 113, no. 2, pp. 112–116, 1991.

[17] S. Ulmer, W. Reinalter, P. Heller, E. Lüpfert, and D. Martínez, “Beam Characterization and Improvement with a Flux Mapping System for Dish Concentrators,” *J. Sol. Energy Eng.*, vol. 124, no. 2, p. 182, 2002.

[18] J. Petrasch *et al.*, “A Novel 50 kW 11,000 suns High-Flux Solar Simulator Based on an Array of Xenon Arc Lamps,” *J. Sol. Energy Eng.*, vol. 129, no. 4, p. 405, 2007.

[19] J. Petrasch, “A Free and Open Source Monte Carlo Ray Tracing Program for Concentrating Solar Energy Research,” *Proc. ASME 2010 4th Int. Conf. Energy Sustain.*, pp. 125–132, 2010.

[20] M. Carmo, D. L. Fritz, J. Rgen Mergel, and D. Stolten, “A comprehensive review on PEM water electrolysis,” *Int. J. Hydrogen Energy*, vol. 38, pp. 4901–4934, 2013.

[21] R. García-Valverde, N. Espinosa, and A. Urbina, “Simple PEM water electrolyser model and experimental validation,” *Int. J. Hydrogen Energy*, vol. 37, no. 2, pp. 1927–1938, 2012.

[22] M. E. Lebbal and S. Lecœuche, “Identification and monitoring of a PEM electrolyser based on dynamical modelling,” *Int. J. Hydrogen Energy*, vol. 34, no. 14, pp. 5992–5999, 2009.

[23] H. Gorgun, “Dynamic modelling of a proton exchange membrane (PEM) electrolyzer,” *Int. J. Hydrogen Energy*, vol. 31, no. 1, pp. 29–38, 2006.

[24] A. Awasthi, K. Scott, and S. Basu, “Dynamic modeling and simulation of a proton exchange membrane electrolyzer for hydrogen production,” *Int. J. Hydrogen Energy*, vol. 36, no. 22, pp. 14779–14786, 2011.

[25] D. Guilbert and G. Vitale, “Dynamic emulation of a PEM electrolyzer by time constant based exponential model,” *Energies*, vol. 12, no. 4, 2019.

[26] Z. Abdin, C. J. Webb, and E. M. Gray, “Modelling and simulation of a proton exchange membrane (PEM) electrolyser cell,” *Int. J. Hydrogen Energy*, vol. 40, no. 39, pp. 13243–13257, 2015.

[27] G. Segev, G. Mittelman, and A. Kribus, “Equivalent circuit models for triple-junction concentrator solar cells,” *Sol. Energy Mater. Sol. Cells*, vol. 98, pp. 57–65, 2012.

[28] P. Singh and N. M. Ravindra, “Temperature dependence of solar cell performance - An analysis,” *Sol. Energy Mater. Sol. Cells*, vol. 101, pp. 36–45, 2012.

[29] Y. P. Varshni, “Temperature dependence of the energy gap in semiconductors,” *physica*, vol. 34, no. 1, pp. 149–154, 1967.

[30] I. Vurgaftman, J. R. Meyer, and L. R. Ram-Mohan, “Band parameters for III-V compound semiconductors and their alloys,” *J. Appl. Phys.*, vol. 89, no. 11 I, pp. 5815–5875, 2001.

[31] M. Theristis and T. S. O’Donovan, “Electrical-thermal analysis of III-V triple-junction solar cells under variable spectra and ambient temperatures,” *Sol. Energy*, vol. 118, pp. 533–546, 2015.

[32] Y. S. Muzychka and M. M. Yovanovich, “Laminar forced convection heat transfer in the combined entry region of non-circular ducts,” *J. Heat Transfer*, vol. 126, no. 1, pp. 54–61, 2004.

[33] P. Olivier, C. Bourasseau, and P. B. Bouamama, “Low-temperature electrolysis system modelling: A review,” *Renew. Sustain. Energy Rev.*, vol. 78, pp. 280–300, 2017.

[34] A. C. Olesen, S. H. Frensch, and S. K. Kær, “Towards uniformly distributed heat, mass and charge: A flow field design study for high pressure and high current density operation of PEM electrolysis cells,” *Electrochim. Acta*, vol. 293, pp. 476–495, 2019.

[35] P. Choi, D. G. Bessarabov, and R. Datta, “A simple model for solid polymer electrolyte (SPE) water electrolysis,” *Solid State Ionics*, vol. 175, no. 1–4, pp. 535–539, 2004.

[36] T. E. Springer, T. A. Zawodzinski, and S. Gottesfeld, “Polymer Electrolyte Fuel Cell Model,” *J. Electrochem. Soc.*, vol. 138, no. 8, pp. 2334–2342, 1991.

[37] F. P. Incropera and D. P. DeWitt, “Fundamentals of Heat and Mass Transfer,” p. 890, 2007.

[38] M. L. V. Ramires, C. A. Nieto Castro, Y. Nagasaka, A. Nagashima, M. J. Assael, and W. A. Wakeham, “Standard Reference Data for the Thermal Conductivity of Water,” *J. Phys. Chem. Ref. Data*, vol. 24, no. 3, pp. 1377–1381, 1995.

[39] J. Pátek, J. Hrub, J. Klomfar, M. Součková, and A. H. Harvey, “Reference correlations for thermophysical properties of liquid water at 0.1 MPa,” *J. Phys. Chem. Ref. Data*, vol. 38, no. 1, pp. 21–29, 2009.

[40] NIST., “Thermophysical Properties of Fluid Systems. www.webbook.nist.gov/chemistry/fluid,” 2020.

[41] F. Marangio, M. Santarelli, and M. Calì, “Theoretical model and experimental analysis of a high pressure PEM water electrolyser for hydrogen production,” *Int. J. Hydrogen Energy*, vol. 34, no. 3, pp. 1143–1158, 2009.

[42] C. Y. Biaku, N. V. Dale, M. D. Mann, H. Salehfar, A. J. Peters, and T. Han, “A semiempirical study of the temperature dependence of the anode charge transfer coefficient of a 6 kW PEM electrolyzer,” *Int. J. Hydrogen Energy*, vol. 33, no. 16, pp. 4247–4254, 2008.

[43] T. A. Zawodzinski, J. Davey, J. Valerio, and S. Gottesfeld, “The water content dependence of electro-osmotic drag in proton-conducting polymer electrolytes,” *Electrochim. Acta*, vol. 40, no. 3, pp. 297–302, 1995.

[44] P. Heller, “The Performance of Concentrated Solar Power (CSP) Systems: Analysis, Measurement and Assessment,” *Perform. Conc. Sol. Power Syst. Anal. Meas. Assess.*, pp. 1–290, 2017.

[45] T. Mancini *et al.*, “Dish-stirling systems: An overview of development and status,” *J. Sol. Energy Eng. Trans. ASME*, vol. 125, no. 2, pp. 135–151, 2003.

[46] B. Endrődi *et al.*, “Multilayer Electrolyzer Stack Converts Carbon Dioxide to Gas Products at High Pressure with High Efficiency,” *ACS Energy Lett.*, vol. 4, no. 7, pp. 1770–1777, Jul. 2019.

[47] B. Endrődi *et al.*, “High carbonate ion conductance of a robust PiperION membrane allows industrial current density and conversion in a zero-gap carbon dioxide electrolyzer cell,” *Energy Environ. Sci.*, vol. 13, no. 11, pp. 4098–4105, 2020.

[48] Holmes-Gentle, I., Tembhurne S., Suter, C. and Haussener, S., 2021. Dynamic system modeling of thermally-integrated concentrated PV-electrolysis. International Journal of Hydrogen Energy.